
Article:
Nienhuis, E.T., Marcial, J., Robine, T. et al. (5 more authors) (2020) Effect of Ti4+ on the structure of nepheline (NaAlSiO4) glass. Geochimica et Cosmochimica Acta, 290. pp. 333-351. ISSN 0016-7037

https://doi.org/10.1016/j.gca.2020.09.015

Accepted Manuscript:
Nienhuis, E.T., J. Marcial, T. Robine, C. Le Losq, D.R. Neuville, M.C. Stennett, N.C. Hyatt, and J.S. McCloy, "Effect of Ti^{4+} on the structure of nepheline ($NaAlSiO_4$) glass," *Geochimica et Cosmochimica Acta*, 290, 333-351 (2020). https://doi.org/10.1016/j.gca.2020.09.015

Effect of Ti^{4+} on the Structure of Nepheline ($NaAlSiO_4$) Glass

Emily T. Nienhuis[1], José Marcial[2], Thibaut Robine[3], Charles Le Losq[3], Daniel R. Neuville[3], Martin C. Stennett[4], Neil C. Hyatt[4], John S. McCloy[1,4]

[1]Materials Science and Engineering Program, Washington State University, PO Box 641030, Pullman, WA, 99164-1030

[2]Pacific Northwest National Laboratory, Richland, WA 99352

School of Mechanical and Materials Engineering, Washington State University, PO BOX 642920, Pullman, WA 99164-2920

[3]Géomatériaux, CNRS, Institut de Physique du Globe de Paris, USPC, 1 rue Jussieu, 75252 Paris Cedex 05, France

[4]Department of Materials Science and Engineering, The University of Sheffield, Sir Robert Hadfield Building, Mappin Street, Sheffield, S1 3JD, UK

Corresponding Author: John McCloy john.mccloy@wsu.edu

Abstract

In this study, the effect of Ti^{4+} on the structure of nepheline glass ($NaAlSiO_4$) is investigated as SiO_2 is systematically replaced with TiO_2. Traditionally, TiO_2 is considered to be a nucleating agent for silicate crystallization but can also be incorporated into the glass network in relatively large amounts as either a network former or modifier depending on its coordination with oxygen. To determine the effect of Ti^{4+} on the structure of nepheline glass, X-ray and neutron pair distribution function (PDF) analysis paired with Empirical Potential Structure Refinement (EPSR) were conducted and are supplemented with Raman spectroscopy, electron probe microanalysis, and X-ray absorption spectroscopy (including Extended X-ray Absorption Fine Structure, EXAFS). Through these methods, it has been found that up to 15 mol% (16 wt%) Ti can incorporate into the glass network as a four-fold coordinated species, with a minor contribution of higher coordinated Ti. Between $NaAlTi_{0.1}Si_{0.9}O_4$ and $NaAlTi_{0.2}Si_{0.8}O_4$, EXAFS suggests a local structure change in the second coordination sphere of Ti, which changes from Ti-Ti to Ti-Al. Raman spectroscopy also suggests that as Ti content increases, the Na environment becomes more ordered. These results suggest that the Ti activity coefficient and its isotopic fractionation for magnetite and other Ti-bearing minerals should be fairly constant in polymerized melts, such as metaluminous and peraluminous rhyolites.

1.0 Introduction

Ti is found in the 4+ valence state in natural glasses in proportions ranging from ~1 wt% in tektites, fulgurites and obsidians to ~16 wt% in lunar glasses (Cicconi and Neuville, 2019), though in the latter, Ti^{3+} can be present due to a low oxygen fugacity (Krawczynski et al., 2009). Despite being a minor constituent in igneous silicate melts, Ti (hereafter Ti refers to Ti^{4+}) plays a significant role in altering the melt structure and affecting thermodynamic and physical properties (Cormier et al., 2001; Cormier et al., 1998; Gan et al., 1996). For instance, in primitive lunar magmas, large variations in Ti concentration can yield orders of magnitude changes in melt viscosities (Rai et al., 2019). Beyond its effects on melt properties, Ti is also used as a geochemical tracer. For example, Ti isotopes can assist in studying the petrological evolution of igneous rocks (Deng et al., 2019; Greber et al., 2017; Millet et al., 2016). Furthermore, Ti-based thermobarometry methods are important tools for characterization of the temperature-pressure (T-P) conditions in igneous systems (Hayden and Watson, 2007; Hofmann et al., 2013). The latter methods require knowledge of the Ti activity in aluminosilicate melts. Ackerson et al. (Ackerson and Mysen, 2020) recently showed that the Ti activity coefficient is affected by melt composition, and that overestimations of this activity coefficient could lead to underestimations of crystallization temperatures by Ti-based trace-element thermobarometers. Such variation in the Ti activity coefficient in melts is not surprising, as Ti shows a variable coordination environment that impacts its solubility in silicate melts and glasses (Ackerson et al., 2020). Similarly, the use of Ti isotopes for geochemical tracking in igneous systems requires the knowledge of the Ti isotopic fractionation factors, which should vary depending on Ti coordination as they do for iron (Dauphas et al., 2014). The influence of Ti on melt properties also depends upon its coordination and

subsequent structural role (Mysen and Neuville, 1995). A good assessment of Ti coordination and environment in aluminosilicate melts thus is critical for many geochemical applications.

In glasses, which are often used as analogues for studying melt structures, Ti is found in four-fold ($^{[4]}$Ti), five-fold ($^{[5]}$Ti), and six-fold ($^{[6]}$Ti) oxygen coordination. Its role in the glass network depends on its coordination state. $^{[4]}$Ti seems to act as a glass former, whereas $^{[6]}$Ti acts as a modifier (Mysen and Neuville, 1995). $^{[5]}$Ti is hypothesized to act as both a network modifier and a network former due to two distinct types of bonds with oxygen – one capable of forming bridging oxygen bonds and the other a terminal oxygen bond (Farges et al., 1996a; Henderson and St-Amour, 2004). More recently, though, $^{[5]}$Ti has been described primarily as a network former due to its ability to form bridging oxygen with other network forming species within the glass, despite the presence of the terminal oxygen bond (Henderson and St-Amour, 2004; Limbach et al., 2017). The influence of Ti on melt properties thus will vary with its coordination because of the interplay between Ti coordination and structural role.

Glass composition and Ti concentration both influence the Ti coordination and environment in glasses, see for example (Dingwell et al., 1994; Farges et al., 1996b; Hamilton and Cleek, 1958; Henderson and St-Amour, 2004; Limbach et al., 2017; Rao, 1963; Sakka et al., 1989; Yarker et al., 1986). Often, a mixture of two coordination states is reported, this being associated with Ti occupying two distinct structural sites in the glass network. This is referred to as the "two-site model" by (Greegor et al., 1983) and is discussed in terms of the "dual role of titanium" by (Rao, 1963), and is seen as an equilibrium between the two coordination states. In the case of glasses containing only TiO_2 and SiO_2, at low TiO_2 additions, the network is primarily made up of SiO_2 with bridging oxygen, yielding a relatively rigid network. As TiO_2 is added, it serves to alter the network connectivity promoting the formation of $^{[4]}$Ti, through the initial presence of $^{[5]}$Ti

which acts as a modifier to break up the network (Greegor et al., 1983). In glasses containing alkali or alkaline earth oxides, the network is broken up by network modifiers, and non-bridging oxygens are present, which does not necessarily require the initial presence of $^{[5]}$Ti as observed for TiO_2-SiO_2 glasses. The Ti coordination in alkali- or alkaline earth-bearing glasses is dependent upon the relative sizes of the modifier cations. Little direct evidence of $^{[6]}$Ti has been found in single phase glasses, though such a species had been proposed in earlier studies (Henderson et al., 2002), and anatase (crystalline TiO_2 with $^{[6]}$Ti) has been observed to crystallize upon TiO_2 saturation in such glasses (Best and Condrate, 1985).

Overall, the changes in Ti coordination and local environment influence the Ti solubility in glasses. Increased amounts of Ti can be incorporated into glasses containing alkali and alkaline earth oxides as compared with those containing only silica (Gan et al., 1996; Limbach et al., 2017; Yarker et al., 1986). The relative amount of Ti that can be accepted into the glass structure and the Ti coordination are hypothesized to be related by two factors, network rigidity and the amount of free-volume within the network (which must be sufficiently large to accommodate Ti polyhedra of various sizes). Based upon this, $^{[4]}$Ti is likely to be present in an unconstrained network featuring non-bridging oxygen, whereas $^{[5]}$Ti is likely to be observed in a more connected and constrained glass network, as observed recently for low-Na_2O silica glass with TiO_2 (Ackerson et al., 2020). $^{[6]}$Ti likely results from volume constraints within the glass network. Unfortunately, at the moment, there is no clear model of Ti coordination and solubility in aluminosilicate glasses and melts. Not only is Ti relevant to geochemical processes, but it also serves as a nucleating agent in glass-ceramics (Beall et al., 2012; Fernandes et al., 2013; Kajiwara, 1988; Krzmanc et al., 2012) and hence understanding its structural role and subsequent behavior as a function of glass composition represents an element of interest for glass and glass-ceramic technological applications.

To tackle this problem, this study seeks to understand the glass structure of Ti-substituted nepheline ($NaAlSiO_4$) glass; specifically, the local structure and the role of Ti^{4+} within the glass matrix and its ability to substitute for Si^{4+} in the glass network. Nepheline glass is a metaluminous composition and its crystalline mineral counterpart is an important constituent of many igneous rocks. This glass composition is also of interest as its composition resembles that of some of the major components of vitrified high level nuclear waste, in which nepheline can crystallize on cooling depending upon the composition of the nuclear waste and the glass-forming additives (Li et al., 1997). As such, studies have sought to understand the relationship between the structure of nepheline glass and additives to its composition and how they related to its propensity for crystallization (Ahmadzadeh et al., 2017; Deshkar et al., 2017; Marcial et al., 2016; Marcial et al., 2018; Marcial and McCloy, 2019; McCloy et al., 2015). In this study, nepheline glasses incorporating various amounts of Ti through substitution for Si were synthesized. Glasses were characterized through pair distribution function (PDF) analysis obtained from both X-ray and neutron total scattering experiments. Further characterization via Ti K-edge X-ray Absorption Spectroscopy (XAS) and Raman spectroscopy were performed. Through the various complementary techniques utilized in the study, an increased understanding for mechanisms of incorporation and network roles of Ti in tectosilicate glasses, and melts, will be obtained.

2.0 Experimental

2.1 Sample Preparation, Physical, and Chemical Characterization

Glasses were batched from reagent-grade TiO_2 (Sigma Aldrich, >99.8 %), SiO_2 (U.S. Silica), Al_2O_3 (Fisher, >99.0 %), and Na_2CO_3 (Fisher, >99.5 %) to obtain the final compositions shown in **Table 1**. Prior to melting, precursor materials were mixed using an agate mortar and pestle to ensure a homogenous batch. All samples were melted in Pt-Rh crucibles for one hour at

1650 °C in an electric furnace and quenched by dipping the bottom of the crucible into a room temperature water bath. The resulting glasses were crushed using a tungsten-carbide (WC) ring mill for 0.06 minutes. The powdered glasses were then melted again for one hour; a second melt ensured a homogenous melt and glass. Nomenclature of the $NaAlTi_xSi_{1-x}O_4$ glasses is shown as *x*-Ti-NAS, *x* is the mole fraction substitution for Si. All compositions with Ti content up to and including 0.3Ti-NAS formed bulk glasses (**Table 1**). Glasses with a higher Ti content resulted in crystallization of TiO_2 on the glass surface upon quench. In the fully Ti-substituted glass, NAT, a bulk ceramic material was formed. Only single-phase glasses were subjected to the subsequent analyses.

Helium pycnometry was performed with a Micromeritics Acupyc II 1340 gas pycnometer on pieces of glass with masses between 0.5-1.0 g in a 1.0 cm^3 sample chamber that had been calibrated using the manufacturer's standard. Each sample was measured ten times and the results were averaged to obtain the final mass density (**Table 1**). Densities of all glass samples were also measured using the Archimedes method with toluene as the immersion liquid. Toluene was utilized for this method as it does not react with glasses, has a good wetting power, and has a well-known density including temperature dependence. Results represent an average of measurements made on four distinct pieces of glass (**Table 1**).

Chemical compositions of the glasses have been measured by wavelength dispersive spectroscopy (WDS) using a Cameca SX100 electron microprobe (**Table 1**), operated by the CAMPARIS facility at University of Paris VI and calibrated with glass and mineral standards. Measurement conditions were 10 nA current, U=15 kV, and 5 s of counting. Sodium loss is not problematic for nepheline glass, but was avoided by defocusing the beam to ~15 μm and moving during analysis, as per standard protocols. The obtained chemical compositions are the mean of

five individual measurements. Glasses were prepared in polymeric resin, polished, and metallized prior to analysis.

2.2 Total Scattering

A summary of the samples on which the total scattering experiments and atomistic simulations were performed is shown in **Table 2** for reference.

2.2.1 X-Ray Total Scattering

X-ray total scattering measurements were conducted at beamline 6-ID-D at the Advanced Photon Source, Argonne National Laboratory, Chicago, with a wavelength of 0.12355 Å. Measurements were performed on fine powdered glass samples packed in 0.0395" (1.02 mm) inner diameter, 0.0435" (1.105 mm) outer diameter polyimide capillaries and sealed with epoxy. Synchrotron X-ray total scattering experiments were performed on all glass samples except 0.3Ti-NAS. Concurrent with sample measurements, measurements of the detector without an X-ray beam and of an empty capillary were taken in order to accurately subtract the dark current, the background attributed to the capillary, and air scattering. Ceria (CeO_2, NIST Standard) was run as a calibrant to determine sample-to-detector distance, the beam center, and the detector tilt using Fit2D software (Hammersley, 1997). The final output of Fit2D was the intensity as a function of 2θ, $I(2\theta)$.

GudrunX (Soper, 2011) software was used to process the reduced intensity data as a function of diffraction angle, $I(2\theta)$, to the total structure factor, $F(Q)$. GudrunX also performed the Fourier transform of the $F(Q)$ to obtain the Pair Distribution Function (PDF) normalized to single atom scattering, referred to as $g(r)$ in this work. For further definition of the functions used in this study, see (Keen, 2001; Marcial and McCloy, 2019). Densities utilized in GudrunX were determined via He-pycnometry, as described above. A Q-range of 0.04-18.0 $Å^{-1}$ with a step size

of 0.04 $Å^{-1}$ was used as the range for useable data as well as for the final *F(Q).* An *r*-max for the final *g(r)* was set to be 17.0 Å with a step size of 0.02 Å. A Breit-Dirac factor was applied ranging from -5 to -9 (note that these values differ from Marcial et al [(Marcial and McCloy, 2019)] due to the different detector). A top-hat width (for the Lorch function) of 1.7 Å was utilized and 1.25 Å was used as the minimum radius for the Fourier transform. The sample 'tweak factor' (1/packing fraction) was set to 1.5 as the samples were powders and were not packed with 100% efficiency in the capillaries.

2.2.2 Neutron Total Scattering

Neutron total scattering experiments were conducted at the NOMAD (BL-1B) beamline at the Spallation Neutron Source of Oak Ridge National Laboratory. Measurements were performed on fine powdered glass samples packed in 3 mm (outer diameter), 0.1 mm thick fused quartz capillaries. Each sample was measured four times and summed to obtain the final *F(Q)* with a *Q*-range of 0-31.4 $Å^{-1}$. The *I(TOF)* data, where TOF is time-of-flight and *I* is intensity, was transformed to *I(Q)*, where *Q* is momentum transfer in $Å^{-1}$, using a diamond standard to calibrate the sample-to-detector distance. The measured intensity of scattered neutrons was transformed to the differential cross-section by subtraction of the scattered intensity of the container and the multiple scattering contribution, then normalizing to the incoherent scattering signal of an empty vanadium can, neglecting the contribution of diffraction peaks (Neuefeind et al., 2012). Using the formalism of Soper et al., the coherent scattering term of the differential cross-section is referred to as the total-scattering structure factor, *F(Q)* (Keen, 2001; Soper et al., 1989). The structure factor was Fourier transformed to yield the pair distribution function, *g(r)*. A Fourier filter was applied to remove spurious peaks below 1.3 Å, below which no known atomic bonds are present for this

system. For further information on this, the reader is referred elsewhere (Marcial and McCloy, 2019; Neuefeind et al., 2012).

To further analyze the neutron total scattering data, the *first sharp diffraction peak* (FSDP) was analyzed using RingFSDP (Shi et al., 2019). RingFSDP probes the FSDP to obtain distributions of ≤4, 5, and ≥6-membered rings within the glass. For further information on RingFSDP and the mathematical method, the reader is referred to (Shi et al., 2019).

2.2.3 Structure Modeling

Empirical Potential Structure Refinement shell (EPSR) was used to model the experimental *F(Q)*, obtained from neutron and X-ray total scattering experiments, via a co-refinement method where the X-ray and neutron *F(Q)* are simultaneously fit (Soper, 2009). The co-refinement method was performed on NAS, 0.1Ti-NAS, and 0.2Ti-NAS. For 0.3Ti-NAS, only the neutron data was modeled using EPSR (X-ray scattering data from a synchrotron source was not obtained for this sample). The modeled *F(Q)* data was then Fourier transformed by EPSR to obtain the modeled *g(r)* for comparison to the experimentally obtained *g(r)* for both neutron and X-ray data; EPSR does not directly model *g(r)*. The reference potentials shown in **Table 3** and the atom box parameters shown in **Table 4** were defined prior to EPSR simulation. In the EPSR potentials, the parameters ε and σ control the depth and width of the potential energy well, while *M* is the atomic number and *q* the valence of the ion.

Prior to starting the simulation, all atoms were distributed randomly through the atom box. The temperature was then set to 10,000 K and the simulations were run until the internal energy of the system had equilibrated. Once the internal energy had equilibrated, the temperature was dropped to 5,000 K, and then to 300 K. Once the internal energy had equilibrated at 300 K, the reference potentials were refined. Next, the maximum value for the refinement of the total

empirical potential of the system was sequentially increased to 50, 100, 150, 200, and 250 kJ mol^{-1}, allowing for further refinement of the reference potentials. A sequential increase of the empirical potential allowed for a feasible solution for the refinement of the reference potentials, as well as a systematic increase of the internal energy of the atom box, allowing for a best possible fit of the experimental data.

Average coordination numbers were calculated by EPSR by counting the number of nearest neighbors within a user-defined distance window (**Table 5**); distance windows were defined based upon the modeled individual *g(r)*'s. Average coordination numbers were additionally determined through visualization of the inflection point in the *N(r)* curve, called the running coordination number, calculated by EPSR, with $N_{ij}(r)$ being defined as the number of atom type *i* surrounding atom type *j* located at radial distance, *r* (Marcial and McCloy, 2019). The function $N_{ij}(r)$ is an average, such that $N_{ij}(r) = \int_{r_1}^{r_2} 4\pi\rho_A r^2 g_{ij}(r)dr$, where ρ_A is the atomic number density, which was calculated from densities determined through He-pycnometry in this study, and $g_{ij}(r)$ is the partial pair distribution function of components *i* and *j* scaled with either the neutron or X-ray scattering lengths. Not all neutron data sets were modeled due to low amounts of Ti in the glasses, resulting in relatively few Ti atoms in the atom box used for EPSR compared to the total atom count.

2.3 Ti K-edge X-ray Absorption Spectroscopy (XAS)

Ti K-edge X-ray absorption spectroscopy (XAS) was collected at two different synchrotron beamlines. Samples for XAS were dispersed in polyethylene glycol (PEG) with ratios optimized to achieve approximately one absorption length thickness while maintaining a suitable Ti K-edge absorption edge step.

2.3.1 KEK Light Source

Samples were measured in transmission mode on beam line BL-27B at the PF Ring of the Photon Factory synchrotron facility (Tsukuba, Japan), which operates at 2.5 GeV with a 300 mA ring current. BL-27B uses a double crystal Si(111) monochromator with a sagittal focussing mechanism, and the energy range accessible extends from 4 to 20 keV. Beam size was restricted to 1 mm (H) and 3 mm (W) using slits, and the intensity of the incident (I_0) and transmitted (I_t) X-ray intensities were measured using ionization chambers which could be filled with a variety of gases to tailor the absorption in each chamber (Konishi et al., 1996). Spectra were recorded between 4836 and 5700 eV with energy steps of 4 eV (4836 – 4956 eV), 0.25 eV (4956 – 5000 eV), 2 eV (5000 – 5250 eV), and 4 eV (5250 – 5700 eV). An accumulation time of 1 s step^{-1} was used for all regions. For each sample, 3 to 30 spectra were averaged (depending on the Ti concentration) to improve the signal to noise ratio. To ensure accurate energy calibration, a transmission spectrum of a Ti foil was acquired and the position of the first inflection point in the derivative spectrum was set to 4966 eV (Bearden and Burr, 1967). The reference foil was also measured after each sample to check the monochromator energy calibration and provide energy reproducibility, between sets of scans, of ± 0.05 eV.

Spectra were recorded for five glasses (0.075Ti-, 0.1Ti-, 0.2Ti-, and 0.3Ti-NAS) and three crystalline standards. The crystalline standards used were: TiO_2 rutile (Sigma Aldrich) containing Ti^{4+} in octahedral coordination, the mineral fresnoite ($Ba_2SiTi_2O_8$) from Junnila Mine, California (BM.2000,121: sample kindly supplied by the British Natural History Museum) containing Ti^{4+} in five-fold coordination, and $Ni_{2.6}Ti_{0.7}O_4$ spinel synthesised from reagent-grade precursors according to Lager et al. (Lager et al., 1981), which contains Ti^{4+} in tetrahedral coordination. All standards were confirmed to be phase pure by X-ray diffraction.

2.3.2 National Synchrotron Light Source-II

Samples were also measured at the National Synchrotron Light Source II (NSLS-II) at Brookhaven National Laboratory (Upton, New York), beamline 6-BM. Spectra of all six glasses (0.025Ti-, 0.050-Ti, 0.075Ti-, 0.1Ti-, 0.2Ti-, and 0.3Ti-NAS) were collected in both fluorescence and transmission mode. 6-BM utilises a 3-pole wiggler source and delivers X-ray in the energy range between 4.5 and 23 keV. The optical system consists of a parabolic collimating mirror (5 nm Rh on 30 nm Pt), Si(111) and Si(311) monochromators, a toroidal focusing mirror, and a flat Pt-coated harmonic rejection mirror. Several modes of operation are possible on the beamline. For this study, the Si(111) monochromator and an unfocused beam was used; the beam was collimated to 0.5 mm in the vertical and 6 mm in the horizontal using slits. Ionization chambers were used to measure the incident and transmitted X-ray energies in transmission geometry and a SII Vortex ME4 (4-element Si drift) detector was used to simultaneously collect the fluorescence signal. The samples were mounted at 45° to both the incident X-ray beam and the vortex detector. The fluorescence signal was dead-time corrected a previously described (Woicik et al., 2010). Spectra were recorded between 4766 and 5606 eV with energy steps of 10 eV (4766 – 4936 eV), 2 eV (4963 – 4956 eV), 0.25 eV (4956 – 4996 eV), and 0.5 eV (4996 – 5606 eV). An accumulation time of 0.5 s step^{-1} was used for the first three regions and 0.25 s step^{-1} for the final region. For each sample, 6 to 12 spectra were averaged (depending on the Ti concentration) to improve the signal to noise ratio. To ensure accurate energy calibration, a transmission spectrum of a Ti metal foil reference was acquired simultaneously with each sample. The Ti foil was placed downstream of the sample between the transmission (I_t) and reference (I_r) ion chambers.

2.3.3 Data reduction

Data reduction and subsequent analysis was performed using the Demeter suite of programs (Athena, Artemis, and Hephaestus) (Ravel and Newville, 2005a, b), for X-ray Absorption Near Edge Structure (XANES) and Extended X-ray Absorption Fine Structure (EXAFS). Initial processing of the data sets involved using a standard background subtraction and edge step normalisation procedure (Newville, 2001; Ravel and Newville, 2005b). The energy of the first maximum in the derivative of the energy spectrum for the Ti foil in the NSLS-II reference channel was calibrated to 4966.0 eV, and after normalization and energy alignment, direct comparisons between the Ti K-edge XANES for the samples could be made. Each Ti foil measurement made at KEK was aligned to the calibrated NSLS-II foil data and the same energy adjustment was then applied to the corresponding samples or standard. A cubic spline function was used to model the background; this was subtracted from the normalized data.

2.3.4 Pre-edge analysis

The pre-edge is related to electronic transitions occurring between the 1s and 3d energy levels and is a feature common to the K-edge spectra of many transition metals. Lower oxidation states have fewer unfilled 3d levels, so transitions from the 1s levels become less probable and the intensity of this feature becomes less defined; here all Ti cations are assumed to be Ti^{4+}, and only these standards were considered. The normalized height of the pre-edge also decreases significantly as a result of an increase in centro-symmetry (i.e., the pre-edge is less distinct for octahedral than tetrahedral symmetry) (Yamamoto, 2008).

It has been shown that, for many transition metals including Ti, the fitting of the pre-edge to the white line can give information about valence and coordination number in glasses (Chalmin et al., 2009; Farges et al., 1996a; Farges et al., 2005). The glasses and the three standards were

measured, and a fitting routine was applied to analyze the pre-edge features. The standards included representative $^{[6]}Ti^{4+}$ (rutile, TiO_2), $^{[5]}Ti^{4+}$ (fresnoite, $Ba_2TiSi_2O_8$), and $^{[4]}Ti^{4+}$ (spinel, $Ni_{2.6}Ti_{0.7}O_4$). For the pre-edge analysis, a series of Gaussians was fit in the 4960 – 5040 eV range, and the contribution for the pre-edge was extracted (Farges et al., 1996b). From this, the centroid and normalized height were determined, with the energies and heights being distinctive for coordination environments of Ti^{4+}.

2.3.5 EXAFS analysis

Subsequently, energy values in eV were converted to k ($Å^{-1}$) to give the k^3 weighted $\chi(k)$ data. Applying a Fourier transform (FT) to the data yielded a partial radial distribution function (RDF) where peaks represent shells of atoms surrounding the central Ti absorber atom. For each shell of atoms, the path length (R), the thermal parameter (σ^2), and the coordination number (N) were extracted by fitting a suitable starting model to the data.

The local structure around the Ti scatterer was obtained from the XAS by fitting the EXAFS using Artemis software (Ravel and Newville, 2005a, b). The data from KEK was used for the fitting. Determination of the local structure in the glass samples requires an independent determination of the amplitude reduction factor (S_0^2) term in the EXAFS equation (Kelly et al., 2008). First, the amplitude reduction factor S_0^2 (= 0.65 ± 0.03) was obtained by fitting the TiO_2 (rutile) standard using the structure from a crystallographic information file (Baur and Khan, 1971), and computing the scattering paths using FEFF. This refined amplitude reduction factor was then used to fit the glasses 0.3Ti-NAS, 0.2Ti-NAS, 0.1Ti-NAS, and 0.075Ti-NAS.

The first coordination shell of oxygen was modeled using a Ti-O scattering path generated using FEFF and the structural model given in the crystallographic information file (CIF) for $NaTi_2Al_5O_{12}$ (Mumme and Wadsley, 1967). The oxygen coordination number around the Ti

($N_{Ti\text{-}O}$), the change in the Ti-O bond length ($\delta R_{Ti\text{-}O}$), the Debye-Waller thermal factors for oxygen (σ^2_O), and the change in the absorption edge energy (δE_0) were all allowed to refine. This approach returned a satisfactory fit to the intense feature in the low radial distance range of the FT $k^3\chi(k)$ [i.e., $|\chi(R)|$ (Å^{-3})]. In order to fit the spectral features at higher radial distance, three additional scattering paths were added. Two scattering paths, Ti-Al and Ti-Ti, were taken from the $NaTi_2Al_5O_{12}$ model and the third path (Ti-Si) was generated from the Na_2TiSiO_5 CIF (Ziadi et al., 1996). The coordination number was kept fixed at two for these additional contributions. An attempt was made to include a Ti-Na scattering path, but this did not yield an improvement in the fit. For each additional scatterer, $\delta R_{Ti\text{-}i}$ (where $R_{Ti\text{-}i}$ indicates the average interatomic distance for a given Ti-i pair) and σ^2_i were refined simultaneously.

To validate the refined path lengths, the bond valance sum (BVS) approach was used (Brown and Altermatt, 1985). The bond valence was calculated using an observed bond length (r_0') of 1.815 Å and empirical constant (B) of 0.37. The BVS was then calculated by multiplying this value by the number of coordinated oxygens refined in the EXAFS fit. Obtained BVS's were between 3.50 and 3.75, with typical errors of 0.5 – 1.0 valence unit (v. u.), close to the expected 4.0 for Ti^{4+}.

2.4 Raman Spectroscopy

Raman spectra were collected on a Jobin-Yvon Horiba T64000 Triple-spectrometer with confocal system through an Olympus BX40 microscope. Samples were excited using a 488.1 nm Coherent Genesis MX SLM laser running at 500 mW output power. The detector was a liquid nitrogen cooled CCD camera. The spectrometer was calibrated using the 520.7 cm^{-1} line of single crystal Si. The spectral resolution is 0.6 cm^{-1}. Spectra were collected through a 100x objective, from 25 to 1300 cm^{-1}, for count times of 200 s, with three subsequent spectra averaged.

3.0 Results

3.1 Pair Distribution Function Analysis

Pair distribution function (PDF) analysis was performed on a subset of samples, as noted. Neutron total scattering data is shown in **Figure 1**. EPSR simulation fits of both neutron and X-ray obtained *F(Q)*, and the resulting *g(r)*, are shown in **Figure 2**. The partial *g(r)* functions were calculated from the EPSR atom model and are shown in **Figure 3**. These partial $g_{ij}(r)$ functions result in the first peak being a combination of Si-O, Ti-O and Al-O pair correlations, with the Si-O correlations being at a slightly shorter distance than that of Ti-O and Al-O. The Ti-O and Al-O bond lengths are nearly identical in these glasses (i.e., 1.80 – 1.84 Å, see Supplementary Information), but this overlap is not problematic due to the negative scattering length of natural Ti in neutron total scattering experiments (see Supplementary Information). By comparing X-ray and neutron total scattering experiments in an EPSR co-refinement, the Ti local environment can be distinguished from that of Si and Al local environments. Na-O does not contribute to the first peak in the $g_{Na\text{-}O}(r)$, but rather in the second peak, occurring around 2.5 Å.

Through observation of the $g_{ij}(r)$, or partial PDF, bond distance windows were defined and used to calculate the coordination numbers. The resultant calculated coordination numbers are shown in **Table 5**. As a secondary means to determine the coordination numbers of species within the glasses, $N_{ij}(r)$ functions were calculated and plotted; the results are shown in **Figure 3**. The $N_{ij}(r)$ functions are independent of user-defined distance windows; rather, they are derived directly from the partial PDF's by EPSR.

Looking specifically at the EPSR calculated coordination numbers (**Table 5**), the Si-O and Al-O coordination remained approximately equal to four, regardless of the Ti addition to the glass. The Na-O coordination number calculations did not result in one consistent coordination number

for Na. The coordination of Na in NAS (nepheline) glass was approximately six. The Na-O coordination increased in the 0.1Ti and 0.2Ti glasses with a coordination number of 6.23 and 6.50, respectively. In the 0.3Ti glass, the Na-O average coordination decreased below six for an average coordination of 5.46. Coordination numbers determined via this method are dependent upon the user definition of a bond-distance window; too large of a window can result in including atoms that are not directly bonded to the species of interest within the calculation, while too small of a distance window results in excluding atoms of interest.

Comparing these coordination numbers to those shown in the $N_{ij}(r)$ plots, Si, Al, and Ti all have coordination numbers approximately of four, with Ti having a slightly higher average coordination. An average Ti-O coordination number larger than four could indicate a minor contribution of $^{[5]}$Ti or $^{[6]}$Ti (with the majority of atoms present as $^{[4]}$Ti). Looking at the atom model from EPSR, Ti is primarily four-fold coordinated, but in the case of the 0.1Ti atom model, a small amount of $^{[5]}$Ti was observed (**Figure 4A**). The coordination of Na-O in the *N(r)* plots is not as well defined, because the inflection point, which is used to determine the coordination number in these functions, is not as clear and does not plateau in the same way that Si-O, Al-O, and Ti-O do in their respective *N(r)* plots.

Further inspection of the atom models exported from EPSR (**Figure 4)** shows $^{[4]}$Ti tetrahedra linking with $^{[4]}$Al, $^{[4]}$Si, and in some cases other Ti polyhedra through bridging oxygen bonds. These atom models show Na atoms interspersed throughout the Al, Si, and Ti interconnected polyhedral network. In addition to using EPSR to determine bond distances and coordination numbers, the exported atom models were visualized using CrystalMaker (Oxfordshire, UK), using the defined bonding distance windows also used in EPSR. The resulting coordination numbers are also shown in **Table 5**. Atom distributions around Ti for the exported

atom model are shown in **Figure 4**; here the first coordination sphere is shown to consist of oxygen atoms, as indicated by the first peak. The second coordination sphere, or second nearest neighbor, is an overlap of Al, Ti, and Si contributions.

The FSDP shown in the neutron total scattering data (**Figure 2**) was also analyzed using RingFSDP to give distributions of ≤4, 5, and ≥6-membered rings present in the glass. Results are shown in **Table 6**. Overall, there was no evidence of rings with four or fewer network formers in the glasses that were measured using neutron total scattering. As Ti was substituted for Si, the fraction of five-membered rings increased at the expense of ≥6-membered rings. The greatest increase of five-membered rings was between the 0.2Ti and 0.3Ti glasses. Even though there was an increase of five-membered rings in the glasses with increasing Ti, the ≥6-membered rings remain the majority species, as expected for a nepheline glass (Taylor and Brown Jr, 1979).

3.3 Ti K-edge XANES

The normalized Ti K-edge XANES spectra for all the glass samples are offset and compared to mineral standards in **Figure 5.** The XANES region contains qualitative information about the mid-range ordering around the Ti atoms in the glass. The trends observed here suggest there is increased ordering around the Ti atoms with increasing Ti concentration (Farges et al., 1996b; Farges et al., 1997).

Visual inspection of the pre-edge region in the stack plot (**Figure 5a**) indicates that Ti cations in the glass are primarily in a tetrahedral coordination environment similar to that in the spinel structured $Ni_{2.6}Ti_{0.7}O_4$. The centroid energy and peak heights calculated for the standards and the glasses were compared against published results in the literature (Farges et al., 1996b). The standards all sit within the expected regions defined in terms of the local Ti environment (**Figure 6**).

The position of the centroid energy and the peak height suggest that Ti is in a tetrahedral environment in all glasses. This is consistent, within error, with the EXAFS fitting described below. To ensure consistency in the pre-edge analysis, average values for the centroid energy position and the peak height were calculated from the fluorescence and transmission data collected at NSLS-II. Independent fitting of the KEK glass data yield results slightly different, but within the tetrahedral domain. It should be noted that differences in beamline alignment and calibration, and the normalization and fitting procedure used (i.e., fitting Gaussians to the whole XANES spectral envelope versus fitting only the pre-edge feature, see Supplementary Information) can affect the final position on the plot. Nonetheless, the results consistently suggest dominance of $^{[4]}Ti^{4+}$.

The EXAFS fits are shown in **Figure 7,** with other *k*-weighting plots shown in the Supplementary Information, and the refined model parameters are given in **Table 7**. From the final EXAFS structural parameters, it can be observed that the local structure of the glasses changes between 0.1Ti-NAS and 0.2Ti-NAS. For the lower Ti concentrations (0.075Ti and 0.1Ti), the second nearest neighbor (2NN) to the Ti scatterer is another Ti atom, ~2.46 Å, implying Ti clustering in the glass network. Additional neighboring Al and Si distances were refined at ~3.00 Å and ~3.25 Å, respectively. For the larger Ti concentrations (0.2Ti and 0.3Ti), the 2NN for the Ti scatterer is Al at 2.76 Å; a third shell containing Si atoms and Ti in the same coordination sphere (within errors) was refined at ~3.00 Å. This change in local structure qualitatively agrees with the change in the XANES region (see **Figure 5b**) which shows increased structure for 0.3Ti and 0.2Ti, while the glasses with lower Ti appear to overlay each other in that region.

Regarding the possibility of higher coordinated Ti, however, the presence of a small amount of $^{[5]}Ti^{4+}$ and/or $^{[6]}Ti^{4+}$ cannot be ruled out from location on the variagram in **Figure 6**.

Indeed, it has been shown (Farges et al., 1996b) that the calculated 50/50 molar mixtures of 4+5 or 4+6 coordinated Ti lie within the circle shown in **Figure 6** (see also Supplementary Information). The decrease in normalized height without substantial change in centroid energy, from 0.1Ti to 0.2Ti to 0.3Ti, could be interpreted as an increase in 6-coordinated Ti units, for instance. Looking at the bond lengths as obtained from EXAFS analysis (see below), and assuming standard average bond lengths for $^{[4]}Ti^{4+}$-O of 1.838 Å, $^{[5]}Ti^{4+}$-O of 1.909 Å, and $^{[6]}Ti^{4+}$-O of 1.953 Å taken from Table 3 of (Farges et al., 1996b), the observed bond lengths and errors (**Table 7**) 1.84 – 1.85 Å with error of 0.01 – 0.03 Å, up to 40% of higher coordinated species would be possible for bond length of 1.88 Å (see Supplementary Information for calculation). These Ti-O bond lengths are comparable but slightly larger than those obtained by PDF (i.e., 1.82 – 1.84 Å, see Supplementary Information). However, in the PDF analysis, the standard deviations are about twice as large as for the EXAFS. Computed coordination numbers for Ti-O from EXAFS are 3.9 – 4.1 (**Table 7**), increasing from 0.1Ti to 0.2Ti to 0.3Ti, possibly suggesting increasing higher Ti coordination with increasing Ti. With PDF, the coordination numbers do not show a trend with Ti content (**Table 5**), but are in the 3.98 – 4.14 range. Standard deviations on the coordination number are high, ≈0.5 for EXAFS but lower at 0.20 – 0.34 for PDF. Thus while it is likely that a small fraction of higher coordinated Ti is present in the glasses, there does not appear to be a strong trend of changing coordination, and it can be reasonably assumed that the average Ti coordination remains close to tetrahedral for all the glasses studied, but the presence of some 5- or 6-coordinated Ti cannot be ruled out. The short-range order of the glasses is relatively constant across the compositional series.

3.4 Raman Spectroscopy

Raman spectra are shown in **Figure 8**, composed of several bands. A broad band is observed at ~80 cm^{-1}, followed by a small peak located at ~290 cm^{-1}. An intense peak is present at ~490 cm^{-1}, with a small shoulder near 560 cm^{-1}. A large and not very intense peak is observed at ~730 cm^{-1}. A broad band is observed near ~1000 cm^{-1}, and Ti-bearing glasses also show an intense band at 890 cm^{-1}.

Increasing the Ti content in the glass results in several clear changes in Raman signals. First, peaks present in the NAS glass Raman spectrum generally become broader and less defined with Ti addition. The other two noticeable changes with Ti addition are (i) the band at ~290 cm^{-1} becomes more intense and better defined, and (ii) a peak at ~890 cm^{-1} appears and increases in intensity at the expense of the ~1000 cm^{-1} peak originally present in the NAS glass. The relative intensity of the two 890 cm^{-1} and ~1000 cm^{-1} bands is represented as a function of the Ti/(Ti+Si) ratio of the glasses in **Figure 9**, where it can be observed that the relative intensity ratio of the 890 cm^{-1} band does not linearly increase as a function of the Ti/(Ti+Si) ratio and instead follows a logarithmic trend. This indicates that the Raman cross section of the vibration giving the signal near ~890 cm^{-1} is very different to that of the vibrations giving the ~1000 cm^{-1} signal in the NAS glass, and changes with Ti concentration. Additionally, the signal mixture between the two different vibrations is a non-linear process.

4.0 Discussion

4.1 Short Range and Medium Range Ordering through PDF analysis

Through the PDF analysis, it can be concluded that Si and Al are four-coordinated and act as network formers, regardless of the Ti content of the glass; there is no observable change in the

Al-O and Si-O bond distance. This agrees with findings from previous studies of other nepheline-based glass compositions using a similar method with EPSR (Marcial and McCloy, 2019). In terms of the Na environment, the CN~6 agrees with a previous study using Na K-edge XANES, where Na in nepheline glass was assumed to be in five- to six-fold coordination with O, similar to the coordination of Na in the mineral nepheline (Neuville et al., 2004). As the Ti content increased, the Na coordination increased, until the 0.3Ti sample, in which the Na coordination decreased its lowest observed value for this study, as observed from EPSR calculations for a user-defined distance window. Calculations of Na coordination number could also vary due to the relatively disordered local environment of Na because of its role as a charge compensator (in the case of pure nepheline glass) or network modifier.

Comparing this to the $N(r)$ plot for Na-O correlations, the inflection point is not well defined, which indicates that there is not one defined coordination number. The lack of definition of the $N_{Na\text{-}O}(r)$ function could be attributed to two things, (i) Na has a relatively small X-ray cross-section compared with the other species within the glass, and (ii) the Na-O local environment may not be as well defined as a SiO_4 tetrahedron; for example, there could be a variety of bond lengths and coordination associated with Na-O due to a high degree of disorder around the Na atoms. Multiple studies have found that Na, Li, and Ca in aluminosilicate glasses varied considerably in coordination numbers, all of which are modifier or charge compensating species, and there are often discrepancies in coordination numbers for these species in literature (Calas et al., 1987; Deubener et al., 1991; Marcial et al., 2018; Marcial and McCloy, 2019). In the case of Na, it was found that the Na-O coordination number, as determined by PDF, ranges from two to ten, with the majority being between five- and seven-coordinated, and an average of six-fold coordinated (Marcial and McCloy, 2019).

Some discrepancy is visible when comparing the coordination numbers calculated by EPSR discussed previously, and the coordination numbers calculated through CrystalMaker. In particular, the coordination numbers calculated from CrystalMaker are consistently lower than those calculated via EPSR and those observed in the *N(r)* plots (**Figure 3**). This is due to the fact that EPSR averages the final result over a series of ensembles (configurations), and thus gives an averaged overall coordination number. By contrast, when the atom model is exported to CrystalMaker, the model is only representative of one configuration of the EPSR model. Though CrystalMaker shows only one possible configuration, it provides a means for observation of the second coordination sphere. Overall, when taking all methods of PDF analysis represented here, the local structure around Si, Al, and Na does not drastically change in terms of coordination numbers and bond distances with regard to substitution of Ti for Si in the glass-forming series.

In addition to probing the short-range ordering of the glasses with total scattering techniques, conclusions can be drawn for the mid-range ordering within these materials. Information regarding the mid-range ordering can be obtained from analysis of the first diffraction peaks in the *F(Q)* data (**Figures 1** and **2**). Changes in intensity and position of the first peak, commonly referred to as the *first sharp diffraction peak*, have been proposed to be related to changes in the ring structure distribution (Shi et al., 2019), average void sizes (Massobrio and Pasquarello, 2001), pseudo plane interplanar spacing (Wright, 2014), density fluctuations (Mukai et al., 2007; Salmon, 1994), and viscosity changes (Micoulaut and Bauchy, 2013). For example, Shi et al (Shi et al., 2019) ascribed a shift in the first diffraction peak to lower *Q* to larger ring structures or larger voids. Changes in intensity of the peak have also been found to correspond to real space density fluctuations (Salmon, 1994). The neutron total scattering data presented here (**Figure 2**) exhibits an overall decrease in the intensity of the first peak (~2 $Å^{-1}$) and a minor

increase in the intensity of the second peak (~3 $Å^{-1}$) as the Ti content of the glass increases. However, there is not a noticeable shift in position. These observations are consistent with the findings from the ring size distribution calculations (obtained using RingFSDP, **Table 6**) which show little change in the proportion of 5 and ≥6 member rings with increasing Ti addition for most of the glasses studied.

4.2 Structure Implications through Raman spectroscopy

Further insight into the overall glass structure is provided through Raman spectroscopy. Three spectral domains of interest can be considered in **Figure 8**. The first one is the Boson region (< 200 cm^{-1}), where the Boson peak is visible at a Raman shift of ~70 cm^{-1}. Its origin remains controversial but can be assigned to vibrations and librations of network-forming polyhedral units (Buchenau et al., 1986; Greaves et al., 2005; Hehlen et al., 2002), such that it is sensitive to changes at medium range order. The second region is located in the range 200-800 cm^{-1}. In this portion of Raman spectra, signals are assigned to T-O-T inter-tetrahedral vibrations (with T a network forming cation like Si). For the present compensated glasses they are built from vibrations of rings of tetrahedral units (Galeener, 1982; McMillan, 1984; Sharma et al., 1985). Finally, the last region of interest is located between 800 and 1300 cm^{-1}. In aluminosilicate glasses, bands in this domain can be assigned to T-O stretching vibrations in the polyhedral units building the network framework (McMillan, 1984; Mysen et al., 1982; Virgo et al., 1980). In Ti-bearing glasses, the ~890 cm^{-1} peak is assigned to Ti-O vibrations in the glass network (Mysen and Neuville, 1995).

When Ti substitutes for Si, the ~890 cm^{-1} peak assigned to Ti-O vibrations increases in intensity as expected. The mixture between the two Ti-O and (Si,Al)-O stretching signals is non-linear (**Figure 8**), rendering futile any attempts to decompose the signals as a linear mixture of two signals. More information actually is embedded in the increase of the signal near ~290 cm^{-1}. This

band may be assigned to a signal from the alkali metal charge compensator cation in its cage, similarly to what has been previously proposed for network modifier cations (Hehlen and Neuville, 2015). The increase of a similar peak is observed with substitution of Na by K in tectosilicate glasses (Le Losq and Neuville, 2017), a phenomenon accompanied by increasing segregation of alkalis in compensator channels, following the Charge Compensated Random Network (CCRN) model (Greaves and Ngai, 1995). Accordingly, the present observations (**Figure 8**) may indicate that, in the presence of Ti, the Na environment tends to become more organized, with the appearance of more clusters and channels of Na compensator cations in the glass structure. Considering that nodes of non-network former cationic channels are preferential nucleating locations (Dargaud et al., 2012), such organization and segregation of Na may help explaining the fact that TiO_2 is a nucleating agent in aluminosilicate glasses. This will be further promoted by a reorganization of the Na environment in glasses before crystallization, as has already been supported by XANES studies. This is also consistent with the fact that when the TiO_2 content is increased beyond 15 mol%, the glasses of corresponding composition could not be synthesized due to crystallization upon quench.

4.3 Coordination and glass-forming role of Ti

Based on the PDF analysis, it was determined that Ti is primarily $^{[4]}$Ti in the nepheline glass series where Ti is substituted for Si, with some higher coordinated Ti species, such as $^{[5]}$Ti or $^{[6]}$Ti, being present in minor amounts. There is a general lack of data concerning Ti-containing aluminosilicate glasses in literature, but in one study, the local structure of Ti was determined by XANES as the Al content in the glass was increased (Romano et al., 2000). It was found that the addition of Al promotes the formation of $^{[4]}$Ti through destabilization of $^{[5]}$Ti pyramids, as the alkali cations are used to charge compensate the Al^{3+} in $^{[4]}$Al tetrahedra (Romano et al., 2000).

According to the PDF analysis conducted here, Al is four-fold coordinated in all glasses, which requires charge balancing cations, such as Na. This could indicate that in the current system, $^{[4]}$Ti (Henderson and St-Amour, 2004) is promoted by the presence of $^{[4]}$Al. If all Al species are 4-coordinated as suggested by the EPSR data of the PDF analysis, all will require charge compensation, in this case likely by a Na atom. With stoichiometric nepheline glass, $NaAlSiO_4$, the network is theoretically fully polymerized and neutrally charged, meaning all of the $^{[4]}$Al and $^{[4]}$Si tetrahedra have four bridging oxygen atoms and all $^{[4]}$Al tetrahedra are charge compensated by one Na atom. $^{[4]}$Ti does not require charge compensation, though it has also been suggested that $^{[5]}$Ti in sodium silicate glasses does not interact closely with Na (Ackerson et al., 2020). The 1:1 ratio of Na:Al in the nepheline glass formulation, as well as substitution of Ti for network-forming Si, could promote the formation of $^{[4]}$Ti, rather than a higher coordinated species. The average EPSR calculated Ti-O coordination was four, or slightly higher than four, as previously discussed.

For the XAS data, the pre-edge height and energy, as well as the bond length, are consistent with a majority of $^{[4]}$Ti (Farges et al., 1996b). The average pre-edge for all the glasses is similar to the pre-edge in the $Ni_{2.62}Ti_{0.7}O_4$ spinel standard. The XANES region, containing information about the mid-range ordering in the glass around Ti (Farges et al., 1996b; Farges et al., 1997), shows trends suggesting increased ordering with increased Ti concentration, which is consistent with the interpretation of the Raman spectra. It is likely that the second-nearest-neighbors after oxygen in the Ti shell are Na atoms, based on previous modeling of Ti K-edge spectra of silicate glasses (Farges et al., 1996a), at least for the high Ti glasses here.

It has also been found in TiO_2-Al_2O_3-SiO_2 glasses that, when Ti substitutes into the glass network as a former, it has a stronger affinity for Al than for Si due to AlO_4^- requiring charge compensation (Kirschen et al., 1999). In the glasses here, since the Na atoms are used to charge

compensate the AlO_4^- units, the local structure then involves $^{[4]}Ti$ connected to AlO_4 tetrahedra with interspersed Na atoms, indicating an increase of Ti-O-Al bonding as Ti is substituted for Si; this structure is also suggested in the EXAFS fit of **Table 7** for 0.2Ti and 0.3Ti, where Al is the 2NN after oxygen, while at lower Ti concentrations the 2NN is Ti. Differences observed in coordination number between the PDF analysis and XAS can be attributed to the fact that the X-ray and neutron total scattering, and subsequent PDF, do not probe one specific atom, but rather look at the glass as a whole, whereas XAS looks specifically at the Ti local environment.

The influence of Ti on glass formability is compositionally dependent. For the case of $NaAl(Si,Ti)O_4$ glasses studied here, when subjected to traditional melt-quenching, the glass formation region was found to extend to $NaAlTi_{0.3}Si_{0.7}O_4$. Through PDF analysis, XAS, and Raman spectroscopy, it is believed that for the currently considered $NaAl(Si,Ti)O_4$ system, Ti tends to tetrahedrally coordinate with oxygen and substitutes for Si, therefore acting as a network former. Through the analysis of EXAFS data, a shift in the second coordination sphere of Ti was observed as the fraction of Ti increased. This could have implications for the crystallization behavior of these systems in the molten state, in addition to the reorganization of the Na environment as suggested by Raman spectroscopy observations.

Considering that these systems feature Al/(Si+Ti) = 1, in order to maximize the separation of positively charged AlO_4 tetrahedra, Ti would need to substitute directly for Si in the alternating Al-O-Si glass network. The observed tendency for Al to serve as the 2NN to Ti in glasses with higher Ti/Si ratios is consistent with Loewenstein's Al-avoidance rule (Loewenstein, 1954).

5.0 Conclusion

This work sought to identify the effect of TiO_2 on the structure of nepheline glass ($NaAlSiO_4$) via a systematic substitution for SiO_2. Through neutron and X-ray total scattering

experiments paired with EPSR atomistic simulations, Raman spectroscopy, and Ti K-edge XAS, the local environments within the glass were determined. It has been found that the Al and Si local environments remained constant as TiO_2 was introduced into the glass. Na coordination showed a non-linear variation in coordination as TiO_2 content was increased, with an abrupt change between the $NaAlTi_{0.2}Si_{0.8}O_4$ (0.2Ti-NAS) and $NaAlTi_{0.3}Si_{0.7}O_4$ (0.3Ti-NAS) glasses, with additional changes in the Na environment being observed through Raman spectroscopy. Ti was found, via analysis to of the total scattering data, to be coordinated with, on average, approximately four oxygen atoms. XAS shows essentially four-fold coordinated Ti with potentially some higher coordinated Ti. From the pre-edge and bond lengths, a fraction of higher coordinated Ti cannot be ruled out, and EPSR simulation may indicate a small contribution of five-fold coordinated Ti. Overall, up to 15 mol% (16 wt%) TiO_2 can be substituted for SiO_2 in $NaAlSiO_4$ while still maintaining a single-phase glass.

Overall, the results presented here show that the Ti local environment in these glasses is quite similar regardless of Ti concentration. This suggests that the Ti activity coefficient and its isotopic fractionation factors for magnetite and other Ti-bearing minerals should be fairly constant in polymerized melts, like metaluminous and peraluminous rhyolites. Combining this information with results from previous studies (Ackerson et al., 2020; Romano et al., 2000), it appears that Ti coordination will change only upon changing melt polymerization and Al content. A critical step toward constraining such changes thus appears to imply a better characterization of the variations of Ti coordination with the NBO/T parameter (ratio of non-bridging oxygen to tetrahedral cations), for instance.

Acknowledgements

Funding for this project was provided through the by the United States Department of Energy (US DOE) Waste Treatment & Immobilization Plant (WTP) Federal Project Office under the direction of Dr. Albert A. Kruger, contract number 89304017CEM000001. A portion of this research used resources at the Spallation Neutron Source (SNS), a US DOE Office of Science (OS) user facility operated by the Oak Ridge National Laboratory (ORNL); neutron scattering work was granted under ORNL SNS IPTS-21702.1. A portion of this research used resources of the Advanced Photon Source (APS), a US DOE OS user facility operated for the DOE OS by Argonne National Laboratory (ANL) under contract DE-AC02-06CH11357; the authors thank Dr. Xiaofeng Guo for use of his beamtime at the APS, Beamline 6-ID-D. A portion of this research used 6-BM of the National Synchrotron Light Source II (NSLSII), user proposal 301027, a US DOE OS user facility operated for the DOE OS by Brookhaven National Laboratory (BNL) under contract DE-SC0012704. A portion of this research used resources of the Photon Factory Advisory Committee, with beamtime at the High Energy Accelerator Research Organization (Kō Enerugī Kasokuki Kenkyū Kikō or KEK) facility in Tsukuba, Japan; the support of Yoshihiro Okamoto (Japan Atomic Energy Agency) during the experiment is gratefully acknowledged. This work was, in part, performed in the HADES/MIDAS facility at the University of Sheffield, established with financial support of the University of Sheffield, Department of Business, Energy and Industrial Strategy, and the Engineering and Physical Sciences Research Council under grant EP/T011424/1. JSM also gratefully acknowledges support from the US-UK Fulbright Commission for support during his sabbatical at the University of Sheffield. Parts of this work were supported by IPGP multidisciplinary program PARI, and by Region île-de-France SESAME Grant no. 12015908.

Supplementary Material

Supplementary information is provided with this article. Additionally, research data is archived at DOI:10.17632/h85yj23ww4.1

References

Ackerson, M.R., Cody, G.D., Mysen, B.O. (2020) ^{29}Si solid state NMR and Ti K-edge XAFS pre-edge spectroscopy reveal complex behavior of Ti in silicate melts. *Prog. Earth Planet. Sci.* **7**, 14.

Ackerson, M.R., Mysen, B.O. (2020) Experimental observations of TiO_2 activity in rutile-undersaturated melts. *Am. Mineral.*, in press, DOI: 10.2138/am-2020-7391.

Ahmadzadeh, M., Marcial, J., McCloy, J. (2017) Crystallization of iron-containing sodium aluminosilicate glasses in the $NaAlSiO_4$-$NaFeSiO_4$ join. *J. Geophys. Res. Solid Earth* **122**, 2504-2524.

Alderman, O., Skinner, L., Benmore, C., Tamalonis, A., Weber, J. (2014) Structure of molten titanium dioxide. *Phys. Rev. B* **90**, 094204.

Baur, W.H., Khan, A.A. (1971) Rutile-type compounds. IV. SiO_2, GeO_2 and a comparison with other rutile-type structures. *Acta Cryst. B* **27**, 2133-2139.

Beall, G.H., American Ceramic, S., Höland, W. (2012) *Glass-ceramic technology*, 2nd ed. ed. American Ceramic Society, Hoboken, N.J.

Bearden, J.A., Burr, A.F. (1967) Reevaluation of X-ray Atomic Energy Levels. *Rev. Mod. Phys* **39**, 125-142.

Bernasconi, A., Dapiaggi, M., Bowron, D., Ceola, S., Maurina, S. (2016) Aluminosilicate-based glasses structural investigation by high-energy X-ray diffraction. *J. Mater. Sci.* **51**, 8845–8860.

Bernasconi, A., Dapiaggi, M., Pavese, A., Bowron, D., Imberti, S. (2012) Local Structure of Si-Al-Ca-Na-O Glasses from Coupled Neutron and X-ray Total Scattering Data. *J. Phys. Chem. B* **116**, 13114-13123.

Best, M.F., Condrate, R.A. (1985) A raman study of TiO_2-SiO_2 glasses prepared by sol-gel processes. *J. Mater. Sci. Lett.* **4**, 994-998.

Brown, I.D., Altermatt, D. (1985) Bond-valence parameters obtained from a systematic analysis of the Inorganic Crystal Structure Database. *Acta Cryst. B* **41**, 244-247.

Buchenau, U., Prager, M., Nücker, N., Dianoux, A.J., Ahmad, N., Phillips, W.A. (1986) Low-frequency modes in vitreous silica. *Phys. Rev. B* **34**, 5665-5673.

Calas, G., Brown, G.E., Waychunas, G.A., Petiau, J. (1987) X-ray absorption spectroscopic studies of silicate glasses and minerals. *Phys. Chem. Mineral.* **15**, 19-29.

Chalmin, E., Farges, F., Brown, G.E. (2009) A pre-edge analysis of Mn K-edge XANES spectra to help determine the speciation of manganese in minerals and glasses. *Contrib. Mineral. Petrol.* **157**, 111-126.

Cicconi, M.R., Neuville, D. (2019) Natural Glasses, in: Musgraves, J.D., Hu, J., Calvez, L. (Eds.), *Springer Handbook of Glass*. Springer, pp. 771-812.

Cormier, L., Calas, G., Neuville, D.R., Bellissent, R. (2001) A high temperature neutron diffraction study of a titanosilicate glass. *J. Non-Cryst. Solids* **293-295**, 510-516.

Cormier, L., Gaskell, P., Calas, G., Soper, A. (1998) Medium-range order around titanium in a silicate glass studied by neutron diffraction with isotropic substitution. *Phys. Rev. B* **58**, 11322-11330.

Dargaud, O., Cormier, L., Menguy, N., Patriarche, G. (2012) Multi-scale structuration of glasses: Observations of phase separation and nanoscale heterogeneities in glasses by Z-contrast scanning electron transmission microscopy. *J. Non-Cryst. Solids* **358**, 1257-1262.

Dauphas, N., Roskosz, M., Alp, E.E., Neuville, D.R., Hu, M.Y., Sio, C.K., Tissot, F.L.H., Zhao, J., Tissandier, L., Médard, E., Cordier, C. (2014) Magma redox and structural controls on iron isotope variations in Earth's mantle and crust. *Earth Planet. Sci. Lett.* **398**, 127-140.

Deng, Z., Chaussidon, M., Savage, P., Robert, F., Pik, R., Moynier, F. (2019) Titanium isotopes as a tracer for the plume or island arc affinity of felsic rocks. *Proc. Nat. Acad. Sci.* **116**, 1132-1135.

Deshkar, A., Marcial, J., Southern, S.A., Kobera, L., Bryce, D.L., McCloy, J.S., Goel, A. (2017) Understanding the structural origin of crystalline phase transformations in nepheline ($NaAlSiO_4$)-based glass-ceramics. *J. Am. Ceram. Soc.* **100**, 2859-2878.

Deubener, J., Sternitzke, M., Mueller, G. (1991) Feldspars $MAlSi_3O_8$ (M = H, Li, Ag) synthesized by low-temperature ion exchange. *Am. Mineral.* **76**, 1620-1627.

Dingwell, D.B., Paris, E., Seifert, F., Mottana, A., Romano, C. (1994) X-ray absorption study of Ti-bearing silicate glasses. *Phys. Chem. Mineral.* **21**, 501-509.

Farges, F., Brown, G.E., Navrotsky, A., Gan, H., Rehr, J.J. (1996a) Coordination chemistry of Ti(IV) in silicate glasses and melts: II. Glasses at ambient temperature and pressure. *Geochim. Cosmochim. Acta* **60**, 3039-3053.

Farges, F., Brown, G.E., Rehr, J.J. (1996b) Coordination chemistry of Ti(IV) in silicate glasses and melts: I. XAFS study of titanium coordination in oxide model compounds. *Geochim. Cosmochim. Acta* **60**, 3023-3038.

Farges, F., Brown, G.E., Rehr, J.J. (1997) Ti K-edge XANES studies of Ti coordination and disorder in oxide compounds: Comparison between theory and experiment. *Phys. Rev. B* **56**, 1809-1819.

Farges, F., Rossano, S., Lefrère, Y., Wilke, M., G. E. Brown, J. (2005) Iron in silicate glasses: a systematic analysis of pre-edge, XANES and EXAFS features. *Physica Scripta* **2005**, 957-959.

Fernandes, H., Tulyaganov, D., Ferreira, J. (2013) The role of P_2O_5, TiO_2 and ZrO_2 as nucleating agents on microstructure and crystallization behaviour of lithium disilicate-based glass. *J. Mater. Sci.* **48**, 765-773.

Galeener, F.L. (1982) Planar rings in glasses. *Solid State Comm.* **44**, 1037-1040.

Gan, H., Wilding, M.C., Navrotsky, A. (1996) Ti^{4+} in silicate melts: Energetics from high-temperature calorimetric studies and implications for melt structure. *Geochim. Cosmochim. Acta* **60**, 4123-4131.

Greaves, G., Meneau, F., Majérus, O., Jones, D., Taylor, J. (2005) Identifying Vibrations That Destabilize Crystals and Characterize the Glassy State. *Science* **308**, 1299-1302.

Greaves, G.N., Ngai, K.L. (1995) Relating the atomic structure of alumino-silicate glasses to their ionic transport properties. *J. Non-Cryst. Solids* **192-193**, 405-410.

Greber, N.D., Dauphas, N., Bekker, A., Ptáček, M.P., Bindeman, I.N., Hofmann, A. (2017) Titanium isotopic evidence for felsic crust and plate tectonics 3.5 billion years ago. *Science* **357**, 1271-1274.

Greegor, R.B., Lytle, F.W., Sandstrom, D.R., Wong, J., Schultz, P. (1983) Investigation of TiO_2-SiO_2 glasses by X-ray absorption spectroscopy. *J. Non-Cryst. Solids* **55**, 27-43.

Hamilton, E.H., Cleek, G.W. (1958) Properties of sodium titanium silicate glasses. *J. Res. Nat. Bur. Stand.* **61**, 89-94.

Hammersley, A.P. (1997) *FIT2D: An Introduction and Overview*.

Hayden, L.A., Watson, E.B. (2007) Rutile saturation in hydrous siliceous melts and its bearing on Ti-thermometry of quartz and zircon. *Earth Planet. Sci. Lett.* **258**, 561-568.

Hehlen, B., Courtens, E., Yamanaka, A., Inoue, K. (2002) Nature of the Boson peak of silica glasses from hyper-Raman scattering. *J. Non-Cryst. Solids* **307-310**, 87-91.

Hehlen, B., Neuville, D.R. (2015) Raman Response of Network Modifier Cations in Alumino-Silicate Glasses. *J. Phys. Chem. B* **119**, 4093-4098.

Henderson, G.S., Liu, X., Fleet, M.E. (2002) A Ti L-edge X-ray absorption study of Ti-silicate glasses. *Phys. Chem. Mineral.* **29**, 32-42.

Henderson, G.S., St-Amour, J.C. (2004) A Si K-edge XANES study of Ti containing alkali/alkaline-earth silicate glasses. *Chem. Geol.* **213**, 31-40.

Hofmann, A.E., Baker, M.B., Eiler, J.M. (2013) An experimental study of Ti and Zr partitioning among zircon, rutile, and granitic melt. *Contrib. Mineral. Petrol.* **166**, 235-253.

Kajiwara, M. (1988) Formation and Crystallization of Al_2O_3-TiO_2-SiO_2 Glasses. *Glass Technol.* **29**, 188-192.

Keen, D. (2001) A comparison of various commonly used correlation functions for describing total scattering. *J. Appl. Cryst.* **34**, 172-177.

Kelly, S., Hesterburg, D., Ravel, B. (2008) Analysis of soils and minerals using X-ray absorption spectroscopy, in: Ulery, A.L., Drees, L.R. (Eds.), *Methods of Soil Analysis Part 5: Mineralogical Methods*. Soil Science Society of America, Inc., Madison, WI, pp. 387-463.

Kirschen, M., Decapitani, C., Millot, F., Rifflet, J., Coutures, J.P. (1999) Immiscible silicate liquids in the system SiO_2-TiO_2-Al_2O_3. *Eur. J. Mineral.* **11**, 427-440.

Konishi, H., Yokoya, A., Shiwaku, H., Motohashi, H., Makita, T., Kashihara, Y., Hashimoto, S., Harami, T., Sasaki, T.A., Maeta, H., Ohno, H., Maezawa, H., Asaoka, S., Kanaya, N., Ito, K., Usami, N., Kobayashi, K. (1996) Synchrotron radiation beamline to study radioactive materials at the Photon factory. *Nucl. Instr. Methods A* **372**, 322-332.

Krawczynski, M.J., Sutton, S.R., Grove, T.L., Newville, M. (2009) Titanium oxidation state and coordination in the lunar high-titanium glass source mantle, *Lunar and Planetary Science Conference*. Lunar and Planetary Science Institute, Houston, TX.

Krzmanc, M., Dosler, U., Suvorov, D. (2012) Effect of a TiO_2 Nucleating Agent on the Nucleation and Crystallization Behavior of MgO-B_2O_3-SiO_2 Glass. *J. Am. Ceram. Soc.* **95**, 1920-1926.

Lager, G.A., Armbruster, T., Ross, F.K., Rotella, F.J., Jorgensen, J.D. (1981) Neutron powder diffraction study of defect spinel structures: Tetrahedrally coordinated Ti^{4+} in $Ni_{2.62}Ti_{0.69}O_4$ and $Ni_{2.42}Ti_{0.74}Si_{0.05}O_4$. *J. Appl. Crystallogr.* **14**, 261-264.

Le Losq, C., Neuville, D.R. (2013) Effect of the Na/K mixing on the structure and the rheology of tectosilicate silica-rich melts. *Chem. Geol.* **346**, 57-71.

Le Losq, C., Neuville, D.R. (2017) Molecular structure, configurational entropy and viscosity of silicate melts: Link through the Adam and Gibbs theory of viscous flow. *J. Non-Cryst. Solids* **463**, 175-188.

Li, H., Vienna, J.D., Hrma, P., Smith, D.E., Schweiger, M.J. (1997) Nepheline precipitation in high-level waste glasses: compositional effects and impact on the waste form acceptability, in: Gray, W.J., Triay, I.R. (Eds.), *Proceedings of MRS*. Materials Research Society, Pittsburgh, PA, pp. 261-268.

Limbach, R., Karlsson, S., Scannell, G., Mathew, R., Edén, M., Wondraczek, L. (2017) The effect of TiO_2 on the structure of Na_2O-CaO-SiO_2 glasses and its implications for thermal and mechanical properties. *J. Non-Cryst. Solids* **471**, 6-18.

Loewenstein, W. (1954) The distribution of aluminum in the tetrahedra of silicates and aluminates. *Am. Mineral.* **39**, 92-96.

Marcial, J., Crum, J., Neill, O., McCloy, J. (2016) Nepheline structural and chemical dependence on melt composition. *Am. Mineral.* **101**, 266-276.

Marcial, J., Kabel, J., Saleh, M., Washton, N., Shaharyar, Y., Goel, A., McCloy John, S. (2018) Structural dependence of crystallization in glasses along the nepheline ($NaAlSiO_4$) - eucryptite ($LiAlSiO_4$) join. *J. Am. Ceram. Soc.* **101**, 2840-2855.

Marcial, J., McCloy, J. (2019) Role of short range order on crystallization of tectosilicate glasses: A diffraction study. *J. Non-Cryst. Solids* **505**, 131-143.

Massobrio, C., Pasquarello, A. (2001) Origin of the first sharp diffraction peak in the structure factor of disordered network-forming systems: Layers or voids? *J. Chem. Phys.* **114**, 7976-7979.

McCloy, J., Washton, N., Gassman, P., Marcial, J., Weaver, J., Kukkadapu, R. (2015) Nepheline crystallization in boron-rich alumino-silicate glasses as investigated by multi-nuclear NMR, Raman, & Mössbauer spectroscopies. *J. Non-Cryst. Solids* **409**, 149-165.

McMillan, P. (1984) Structural studies of silicate glasses and melts: applications and limitations of Raman spectroscopy. *Am. Mineral.* **69**, 622-644.

Micoulaut, M., Bauchy, M. (2013) Anomalies of the first sharp diffraction peak in network glasses: Evidence for correlations with dynamic and rigidity properties. *phys. status. solidi (b)* **250**, 976-982.

Millet, M.-A., Dauphas, N., Greber, N.D., Burton, K.W., Dale, C.W., Debret, B., Macpherson, C.G., Nowell, G.M., Williams, H.M. (2016) Titanium stable isotope investigation of magmatic processes on the Earth and Moon. *Earth Planet. Sci. Lett.* **449**, 197-205.

Mukai, A., Kohara, S., Uchino, T. (2007) Modification of medium-range order in silica glass by ball-milling: real- and reciprocal-space structural correlations for the first sharp diffraction peak. *J. Phys. Cond. Matt.* **19**, 455214.

Mumme, W.G., Wadsley, A.D. (1967) The crystal structure of $NaTi_2Al_5O_{12}$. *Acta Cryst.* **23**, 754-758.

Mysen, B., Neuville, D. (1995) Effect of temperature and TiO_2 content on the structure of $Na_2Si_2O_5$ $Na_2Ti_2O_5$ melts and glasses. *Geochim. Cosmochim. Acta* **59**, 325-342.

Mysen, B.O., Virgo, D., Seifert, F.A. (1982) The structure of silicate melts: Implications for chemical and physical properties of natural magma. *Rev. Geophys.* **20**, 353-383.

Neuefeind, J., Feygenson, M., Carruth, J., Hoffmann, R., Chipley, K.K. (2012) The Nanoscale Ordered Materials Diffractometer NOMAD at the Spallation Neutron Source SNS. *Nucl. Instrum. Methods Phys. Res. B* **287**, 68-75.

Neuville, D., Cormier, L., Flank, A.-M., Prado, R., Lagarde, P. (2004) Na K-edge XANES spectra of minerals and glasses. *Eur. J. Mineral.* **16**, 809-816.

Newville, M. (2001) IFEFFIT : interactive XAFS analysis and FEFF fitting. *J. Synchr. Rad.* **8**, 322-324.

Rai, N., Perrillat, J.-P., Mezouar, M., Colin, A., Petitgirard, S., van Westrenen, W. (2019) In situ Viscometry of Primitive Lunar Magmas at High Pressure and High Temperature. *Front. Earth Sci.* **7**.

Rao, B. (1963) The dual role of titanium in the system K_2O-SiO_2-TiO_2. *Phys. Chem. Glasses* **4**, 22-34.

Ravel, B., Newville, M. (2005a) ATHENA and ARTEMIS: Interactive graphical data analysis using IFEFFIT. *Phys. Scripta* **T115**, 1007-1010.

Ravel, B., Newville, M. (2005b) ATHENA, ARTEMIS, HEPHAESTUS: data analysis for X-ray absorption spectroscopy using IFEFFIT. *J. Synchr. Rad.* **12**, 537-541.

Romano, C., Paris, E., Poe, B., Giuli, G. (2000) Effect of aluminum on Ti-coordination in silicate glasses: A XANES study. *Am. Mineral.* **85**, 108-117.

Sakka, S., Miyaji, F., Fukumi, K. (1989) Structure of Binary K_2O-TiO_2 and Cs_2O-TiO_2 Glasses. *J. Non-Cryst. Solids* **112**, 64-68.

Salmon, P.S. (1994) Real space manifestation of the first sharp diffraction peak in the structure factor of liquid and glassy materials. *Proc. Royal Soc. London A: Math. Phys. Sci.* **445**, 351-365.

Sharma, S.K., Philpotts, J.A., Matson, D.W. (1985) Ring distributions in alkali- and alkaline-earth aluminosilicate framework glasses- a Raman spectroscopic study. *J. Non-Cryst. Solids* **71**, 403-410.

Shi, Y., Neuefeind, J., Ma, D., Page, K., Lamberson, L.A., Smith, N.J., Tandia, A., Song, A.P. (2019) Ring size distribution in silicate glasses revealed by neutron scattering first sharp diffraction peak analysis. *J. Non-Cryst. Solids* **516**, 71-81.

Soper, A. (2011) *GudrunN & GudrunX: Programs for correcting raw neutron and X-ray diffraction data to differential scattering cross section*.

Soper, A., Howells, W., Hannon, A. (1989) *ATLAS - Analysis of Time-of-Flight Diffraction Data from Liquid and Amorphous Samples*. Rutherford Appleton Laboratory.

Soper, A.K. (2009) Empirical Potential Structure Refinement- EPSR Shell.

Taylor, M., Brown Jr, G.E. (1979) Structure of mineral glasses—II. The SiO_2-$NaAlSiO_4$ join. *Geochim. Cosmochim. Acta* **43**, 1467-1473.

Virgo, D., Mysen, B.O., Kushiro, I. (1980) Anionic Constitution of 1-Atmosphere Silicate Melts: Implications for the Structure of Igneous Melts. *Science* **208**, 1371-1373.

Woicik, J.C., Ravel, B., Fischer, D.A., Newburgh, W.J. (2010) Performance of a four-element Si drift detector for X-ray absorption fine-structure spectroscopy: resolution, maximum count rate, and dead-time correction with incorporation into the ATHENA data analysis software. *J. Synchr. Rad.* **17**, 409-413.

Wright, A.C. (2014) Crystalline-like ordering in melt-quenched network glasses? *J. Non-Cryst. Solids* **401**, 4-26.

Yamamoto, T. (2008) Assignment of pre-edge peaks in K-edge -ray absorption spectra of 3d transition metal compounds: electric dipole or quadrupole? *X-Ray Spectrom.* **37**, 572-584.

Yarker, C.A., Johnson, P.A.V., Wright, A.C., Wong, J., Greegor, R.B., Lytle, F.W., Sinclair, R.N. (1986) Neutron diffraction and EXAFS evidence for TiO_5 units in vitreous K_2O-TiO_2-$2SiO_2$. *J. Non-Cryst. Solids* **79**, 117-136.

Ziadi, A., Hillebrecht, H., Thiele, G., Elouadi, B. (1996) Crystal Structure of Orthorhombic LT-Na_2TiSiO_5 and Its Relation to the Tetragonal HT-Form. *J. Solid State Chem.* **123**, 324-330.

Tables

Table 1. Sample names, compositions (nominal and analyzed), and mass densities of glasses used in this study

Sample	Composition	Oxides (mol%) nominal				Oxides (wt%) analyzed				Density, Archim. (g/cm^3)	Density, Pycnom. (g/cm^3)
		Na_2O	Al_2O_3	SiO_2	TiO_2	Na_2O	Al_2O_3	SiO_2	TiO_2		
NAS	$NaAlSiO_4$	25.0	25.0	50.0	0.0	21.42(0.05)	35.95(0.59))	40.58(0.80)	0.00(0.02)	2.490(1)	2.4923
0.025Ti-NAS	$NaAlTi_{0.025}Si_{0.975}O_4$	25.0	25.0	48.75	1.25	19.70(0.15)	35.86(0.09)	39.80(0.42)	1.43(0.06)	2.500(2)	2.5111
0.050Ti-NAS	$NaAlTi_{0.050}Si_{0.950}O_4$	25.0	25.0	47.5	2.5	19.68(0.20)	36.06(0.29)	38.99(0.41)	2.85(0.05)	2.496(4)	2.4923
0.075Ti-NAS	$NaAlTi_{0.075}Si_{0.925}O_4$	25.0	25.0	46.25	3.75	19.51(0.07)	35.54(0.09)	38.08(0.36)	4.29(0.07)	2.510 (1)	2.5083
0.1Ti-NAS	$NaAlTi_{0.1}Si_{0.9}O_4$	25.0	25.0	45.0	5.0	18.94(0.07)	35.30(0.26)	37.18(0.72)	5.71(0.06)	2.515 (5)	2.5016
0.2Ti-NAS	$NaAlTi_{0.2}Si_{0.8}O_4$	25.0	25.0	40.0	10.0	18.25(0.22)	35.17(0.09)	32.92(0.35)	11.16(0.14)	2.559(1)	2.5503
0.3Ti-NAS	$NaAlTi_{0.3}Si_{0.7}O_4$	25.0	25.0	35.0	15.0	17.62(0.18)	35.15(0.23)	29.07(0.49)	16.64(0.12)	2.614(3)	2.6048
0.4Ti-NAS*	$NaAlTi_{0.4}Si_{0.6}O_4$	25.0	25.0	30.0	20.0	n/a	n/a	n/a	n/a	n/a	n/a
0.5Ti-NAS*	$NaAlTi_{0.5}Si_{0.5}O_4$	25.0	25.0	25.0	25.0	n/a	n/a	n/a	n/a	n/a	n/a
NAT*	$NaTiSiO_4$	25.0	25.0	0.0	50.0	n/a	n/a	n/a	n/a	n/a	n/a

*Resulted in crystallization upon quench; did not produce a single-phase glass. Therefore, they were not analyzed by EPMA (n/a). Neither were their density.

Table 2. A list of samples and the PDF analysis experiments performed for each. See Appendix for description of the lab-scale xPDF measurements

Sample	Neutron PDF	Synchrotron xPDF	Lab-scale xPDF	EPSR	RingFSDP
NAS	x	x	x	x	x
0.025Ti	x	x	x		x
0.050Ti	x	x	x		x
0.075Ti	x	x	x		x
0.1Ti	x	x	x	x	x
0.2Ti	x	x	x	x	x
0.3Ti	x		x	x	x

Table 3. Potentials used in EPSR modeling.

Atom Type	ε (kJ/mole)	σ (Å)	M (amu)	q (e)	Reference
Si	0.8	0.76	28	4.0	(Bernasconi et al., 2012)
Al	0.8	1.2	27	3.0	(Bernasconi et al., 2012)
Na	0.8	2.3	23	1.0	(Bernasconi et al., 2012)
Ti	2.23	1.31	48	4.0	(Alderman et al., 2014)
O	0.65	3.69	16	-2.0	(Bernasconi et al., 2016; Bernasconi et al., 2012)

Table 4. Atom box parameters used in EPSR modeling. Densities shown are from pycnometry

Sample	ρ (g/cm^3)	Na	Al	Si	Ti	O
NAS	2.4923	500	500	500	0	2000
0.1Ti-NAS	2.5016	500	500	450	50	2000
0.2Ti-NAS	2.5503	500	500	400	100	2000
0.3Ti-NAS	2.6048	500	500	350	150	2000

Table 5. Coordination numbers, and standard deviations, as calculated via EPSR and (CrystalMaker), shown in parentheses, through a user defined bond distance window. Distance windows used in the calculation, in Å, are shown as determined through partial g(r)'s.

Sample	Average Coordination Number			
	Al-O	Na-O	Si-O	Ti-O
NAS	4.02±0.023	6.09±0.94	3.95±0.22	-
0.1Ti-NAS	3.93±0.28 (3.65±0.65)	6.23±1.03 (5.53±1.52)	3.94±0.23 (3.66±0.64)	4.14±0.34 (3.88±0.68)
0.2Ti-NAS	3.95±0.25 (3.67±0.62)	6.50±0.99 (5.85±1.48)	3.93±0.206 (3.66±0.64)	3.98±0.20 (3.78±0.58)
0.3Ti-NAS	3.99±0.19 (3.71±0.62)	5.46±1.03 (4.83±1.14)	3.95±0.21 (3.73±0.56)	4.12±0.33 (3.88±0.67)
Distance Window (Å)	1.5-2.3	2.0-3.2	1.3-2.0	1.6-2.2

Table 6. Ring number statistics obtained from analyzing the neutron total scattering data with RingFSDP.

Sample	% 5-membered	% ≥6-membered	Avg. Medium Range Distance (Å)
NAS	27.08	72.92	4.138
0.025Ti-NAS	26.87	73.13	4.139
0.05Ti-NAS	27.08	72.92	4.137
0.075Ti-NAS	27.36	72.64	4.136
0.1Ti-NAS	27.86	72.14	4.133
0.2Ti-NAS	29.45	70.55	4.124
0.3Ti-NAS	32.72	67.28	4.104

Table 7. Structural parameters for Ti-containing glasses obtained from modeling Ti K-edge EXAFS. $R_{Ti\text{-}i}$ is the average interatomic distance for a given Ti-i pair, σ^2_i is the EXAFS Debye-Waller factor (estimated from the distribution of bond length) and $N_{Ti\text{-}O}$ is the refined number of scatterers in the first oxygen coordination shell which was allowed to refine. The number of scatterers in all other shells were fixed during the fits to 2 each for Al, Ti, and Si, i.e. $N_{Ti\text{-}Ti} = N_{Ti\text{-}Al} = N_{Ti\text{-}Si} = 2.0$. The amplitude reduction factor (S_0^2), determined from the fitting of the TiO_2 rutile reference, was fixed at $S_0^2 = 0.65$. BVS is the bond valence sum for the first oxygen coordination shells.

	0.075Ti-NAS		**0.1Ti-NAS**		**0.2Ti-NAS**		**0.3Ti-NAS**	
		±		±		±		±
E_0 (eV)	0.72	3.54	-0.35	2.15	-2.9	1.7	-3.09	1.80
$R_{Ti\text{-}O}$ (Å)	1.85	0.03	1.85	0.02	1.84	0.01	1.85	0.01
$N_{Ti\text{-}O}$	3.87	0.74	3.85	0.46	3.99	0.45	4.11	0.47
σ^2_O (Å^2)	0.009	0.003	0.007	0.002	0.006	0.012	0.008	0.002
$R_{Ti\text{-}Ti}$ (Å)	2.46	0.03	2.46	0.02	3.02	0.05	3.02	0.05
σ^2_{Ti} (Å^2)	0.013	0.003	0.017	0.004	0.004	0.007	0.004	0.006
$R_{Ti\text{-}Al}$ (Å)	2.96	0.09	3.00	0.08	2.76	0.04	2.76	0.04
σ^2_{Al} (Å^2)	0.016	0.014	0.017	0.011	0.014	0.007	0.013	0.006
$R_{Ti\text{-}Si}$ (Å)	3.25	0.04	3.25	0.03	2.99	0.06	2.98	0.05
σ^2_{Si} (Å^2)	0.005	0.005	0.005	0.003	0.001	0.007	0.001	0.005
R factor	0.037	-	0.015	-	0.018	-	0.018	-
BVS (v.u.)	3.52	1.03	3.50	0.23	3.73	0.53	3.74	0.54

Figures

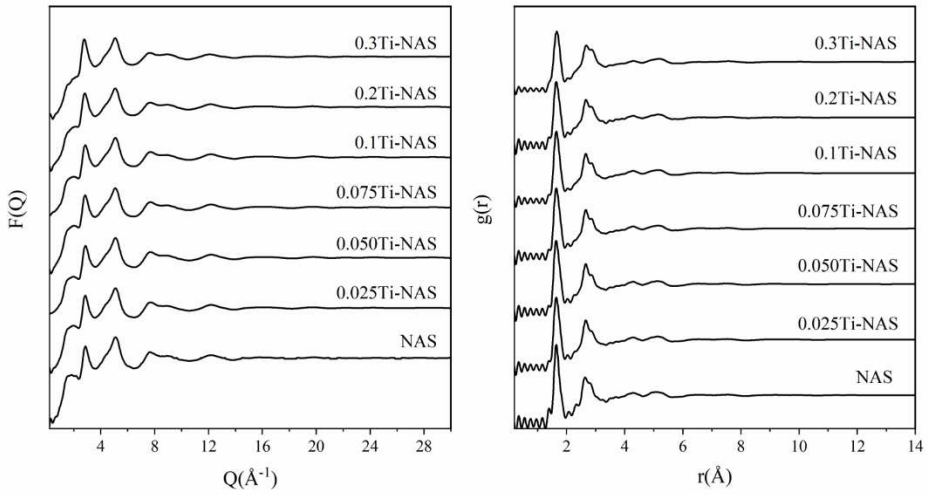

Figure 1. Experimental *F(Q)* and *g(r)* as obtained through neutron total scattering experiments.

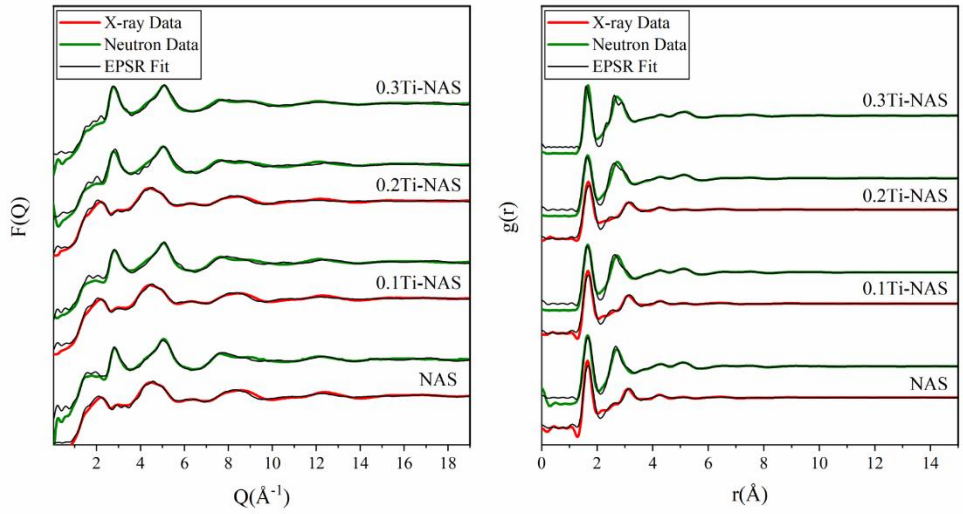

Figure 2. Comparison of experimental and EPSR simulation *F(Q)* (left) and *g(r)* (right) for neutron and X-ray data. Note that the *g(r)* data shown is a Fourier Transform, performed by EPSR, of the experimental data.

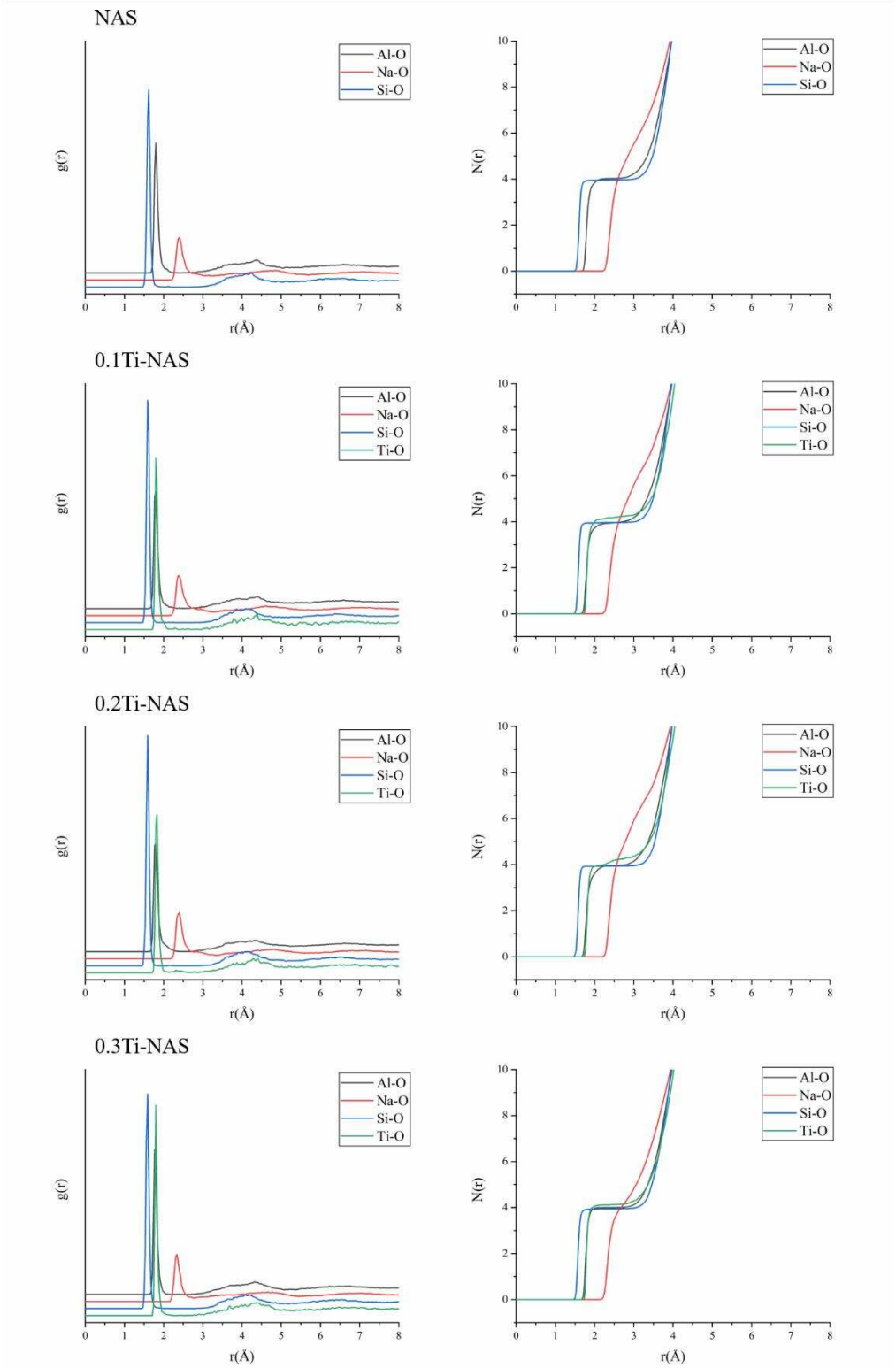

Figure 3. Partial (deconvoluted) *g(r)* and *N(r)* plots obtained through EPSR simulation. The inflection/plateau in the *N(r)* plots gives the average coordination number of the species.

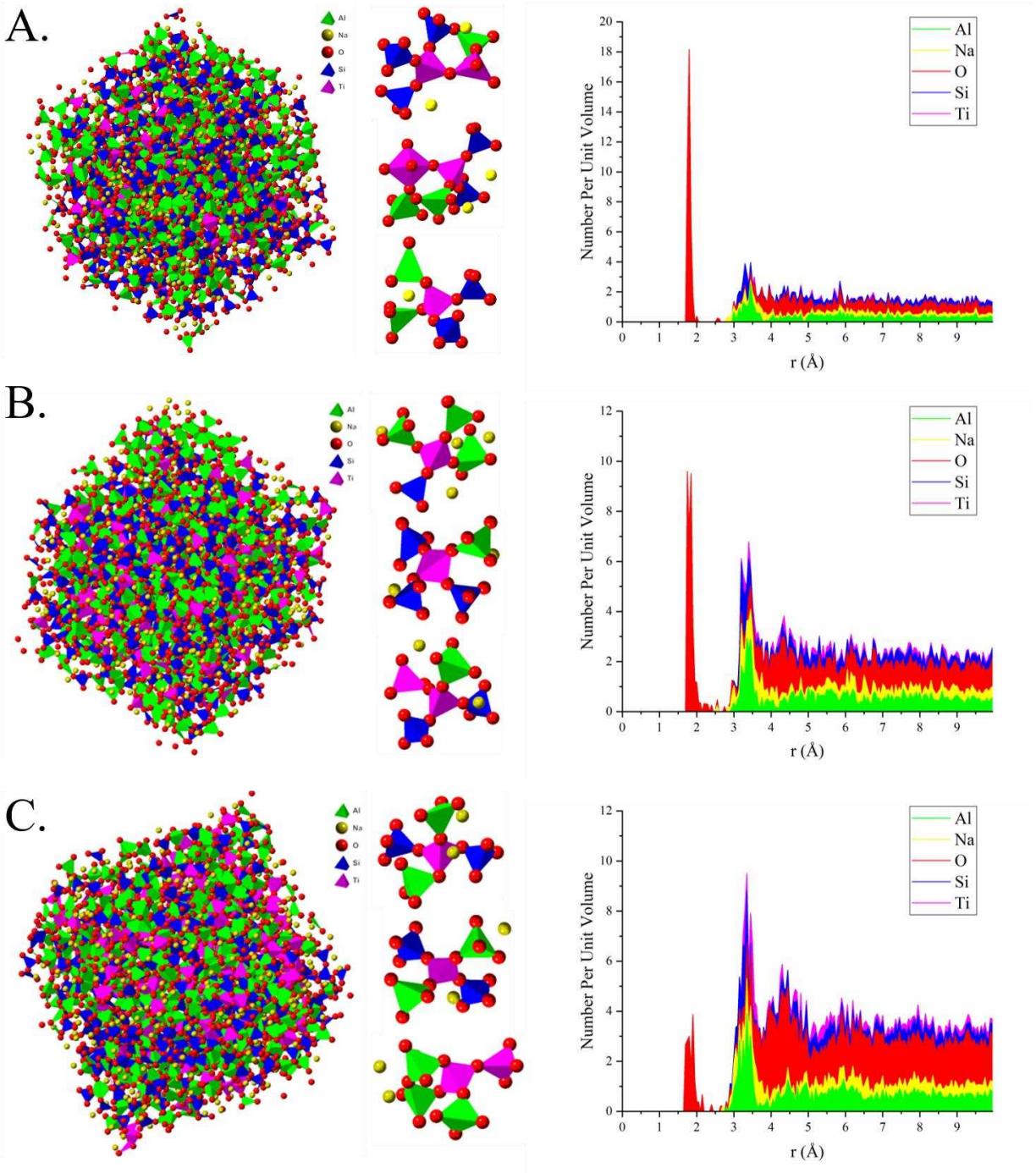

Figure 4. Exported atom models, with sample Ti environments, from EPSR and the subsequent bond distributions from CrystalMaker. A.) atom model for 0.1Ti; B.) atom model for 0.2Ti; C.) atom model for 0.3Ti.

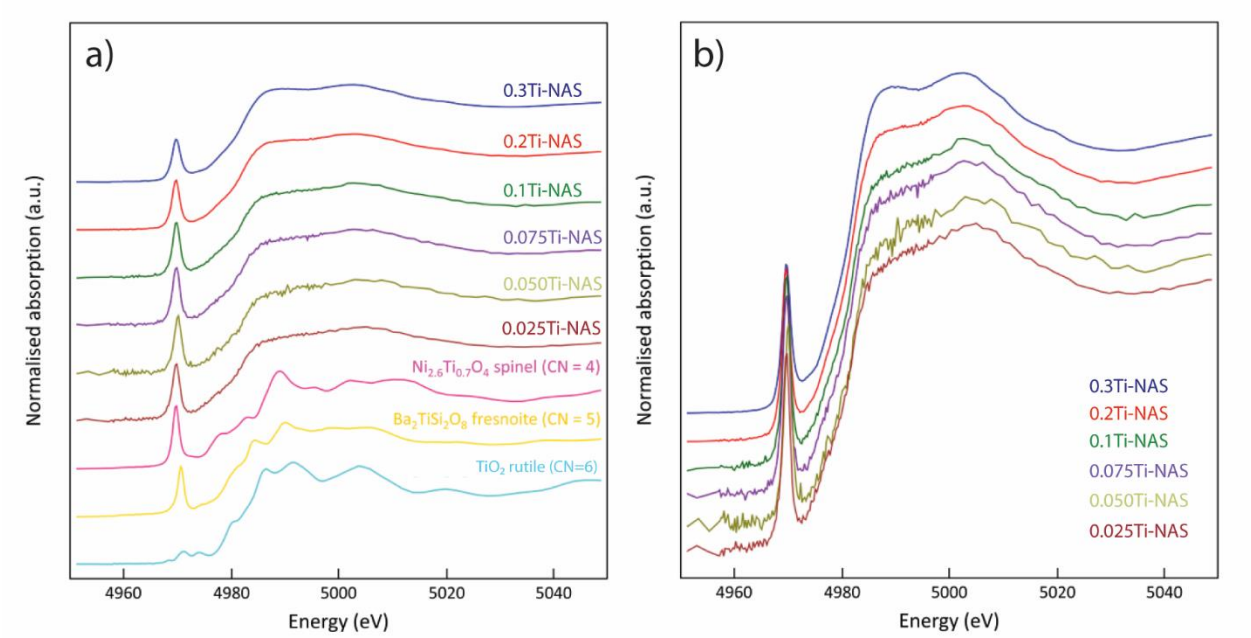

Figure 5. XANES region measurements for the Ti K-edge XAS. Standards shown were measured at KEK in transmission. Glasses shown were measured at NSLS-II in transmission, and are representative of the other measurements of the glasses at KEK in transmission and NSLS-II in fluorescence.

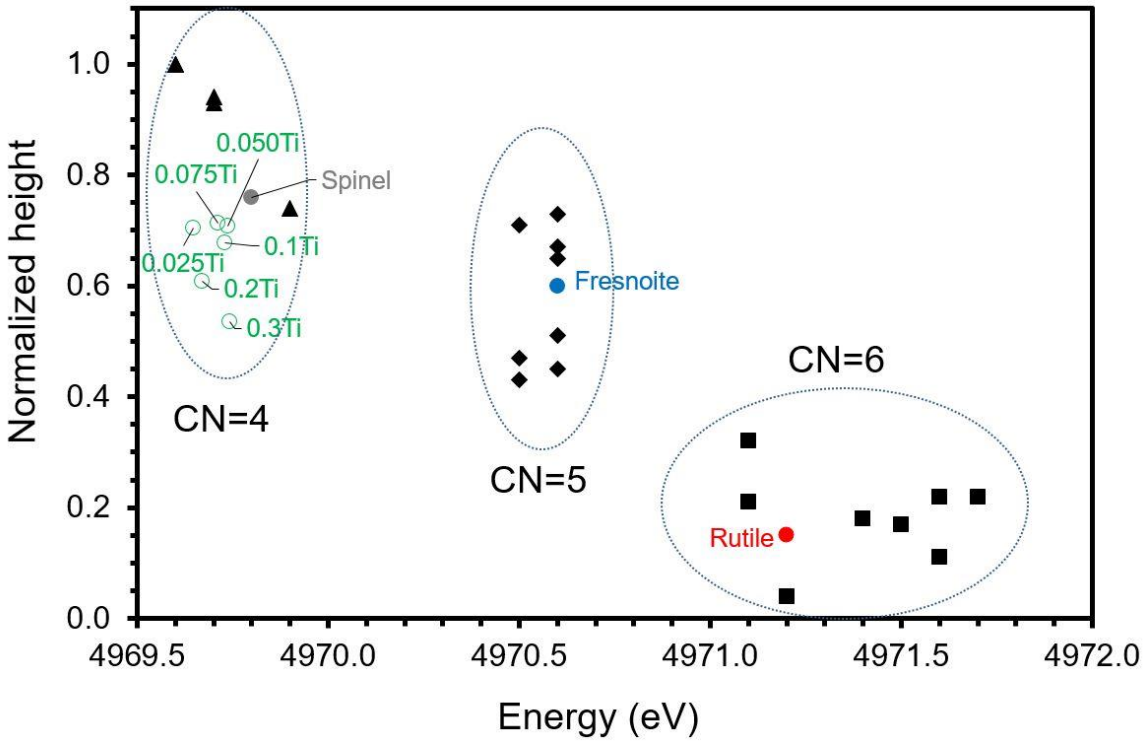

Figure. 6. Energy versus normalized height for the crystalline standards [labeled: rutile, (TiO_2), fresnoite, ($Ba_2TiSi_2O_8$), spinel, ($Ni_{2.6}Ti_{0.7}O_4$)], the glasses, and other crystalline materials having characteristic pre-edge features (from Farges et al (Farges et al., 1996b)). Data obtained for standards at KEK in transmission, and for glasses at NSLS-II (average of fits to transmission and fluorescence pre-edge data).

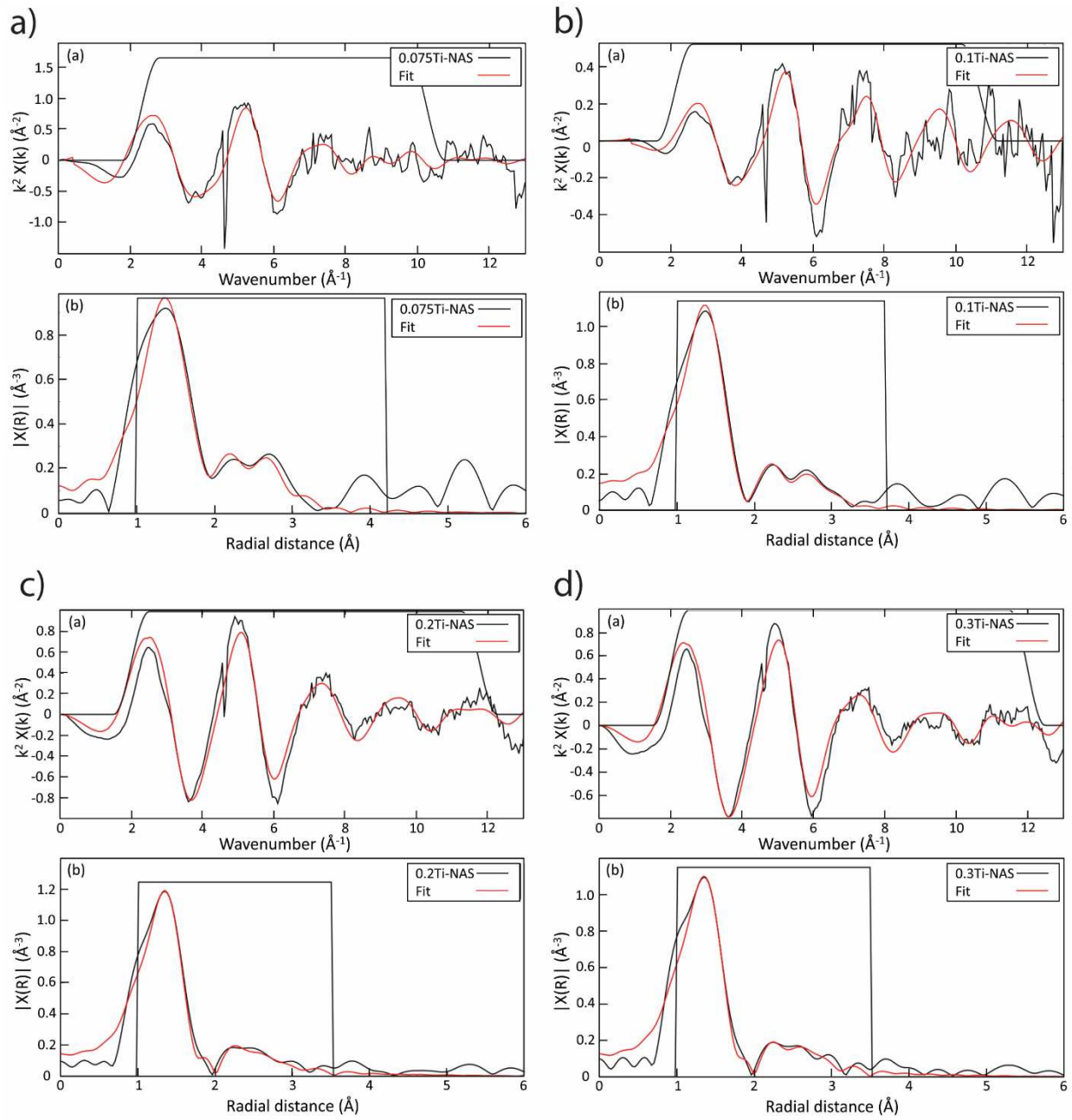

Figure. 7. EXAFS fits for a.) 0.075Ti-NAS; b.) 0.1Ti-NAS; c.) 0.2Ti-NAS; d.) 0.3Ti-NAS.

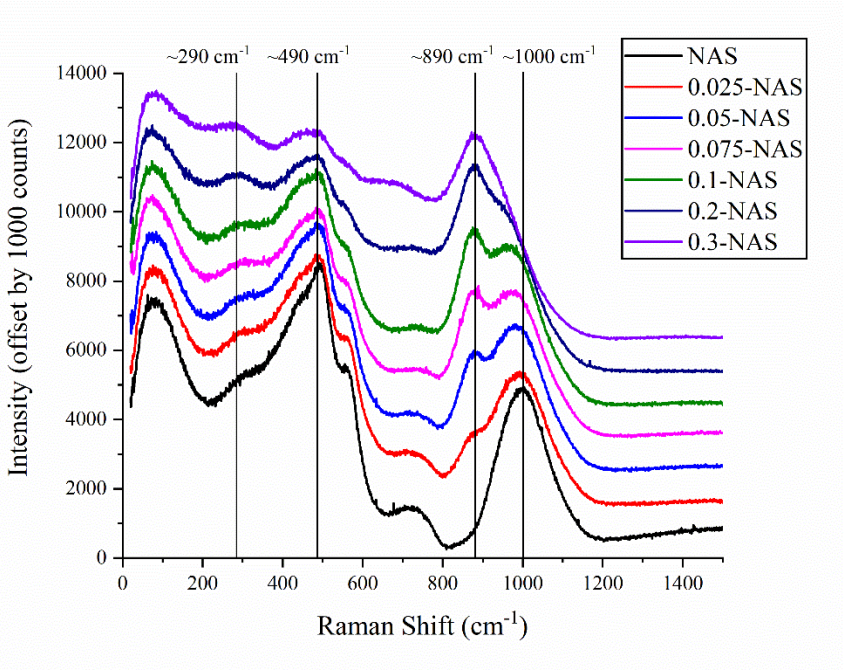

Figure 8. As-measured Raman spectra of Ti-NAS glass, without any background subtraction or normalization; spectra are offset for clarity

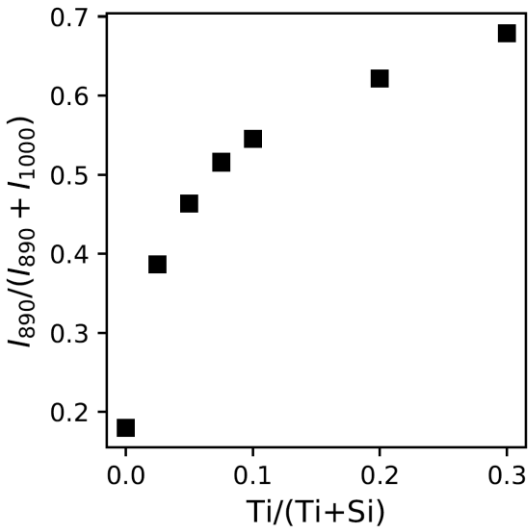

Figure 9. Relative intensities of the 890 cm^{-1} Raman bands to the 1000 cm^{-1} bands of the glasses as a function of the Ti/(Ti+Si) ratio in the glass.